Egyptian Geophysical Society
EGS Journal, Vol. 15, No. 1, 47-73 (2017)

A GEOLOGICAL-GEOCHEMICAL-GEOPHYSICAL INTEGRATED STUDY ON UMM NAR IRON ORE FROM THE CENTRAL EASTERN DESERT OF EGYPT

S.R. Hassan[(1)], M.M. Hamdy[(2)], E.A. Issawy[(1)], A.A. El-Boghdady[(3)] and A.M. Radwan[(1)]

(1) National Research Institute of Astronomy and Geophysics, Helwan, Cairo, Egypt.
(2) Geology Department, Faculty of Science, Tanta Univ., Tanta, Egypt.
(3) Geology Department, Faculty of Science, Menofia Univ., Sheeben Elkoom, Egypt.

دراسة جيولوجية، جيوكيميائية وجيوفيزيقية تكاميلية لخام حديد أم نار- الجزء الأوسط من الصحراء الشرقية، مصر

الخلاصـــة: تحتوى تكوينات الحديد الشرائطية على أكثر من ١٥ ٪ من محتويات الحديد ذى النشأة الرسوبية، ولهذه التكوينات أهمية اقتصادية كبيرة حيث كثيرا ما تحتوي نسبة عالية من الحديد بالإضافة الي الذهب. وتعد تكوينات الحديد الشرائطية بمنطقة أم النار من أقدم وأكبر الوحدات الصـــخرية ذات النشأة الرسوبية والتكتونية منذ عصر ما قبل الكامبرى بالصحراء الشرقية بمصر والتأثر بمراحل تشوه متعددة أثناء وبعد غلق محيط الموزامبيقي البروتيروزوي المتأخر، مكونة مجموعات مختلفة من الصدوع والطي . ولهذا فقد تم اختيار راسب حديد أم نار لإجراء دراسة جيولوجية- جيوكيميائية- جيوفيزيقية (التثاقلية والمغناطيسية الأرضية) متكاملة يمكن فيها تحديد امتداد خام الحديد وعمقه وتأثير التراكيب الجيولوجية في توزيع العناصر الكيميائية المكونة للراسب المعدني كذلك إيجاد العلاقة بين تركيز الحديد وغيره من تمعدنات متوقعة مثل الذهب.

اشتملت الدراسة على وصف حقلي وبتروجرافي وتحديد التركيب المعدني والجيوكيميائى (للعناصر الأساسية والشحيحة) لخام الحديد المكشوف سطحيا أما المسح الجيوفيزيائى فقد اشتمل على تجميع حقلى لبيانات التثاقلية الأرضية باستخدام جهاز قياس التثاقلية الأرضية (CG5- Gravimeter) وبيانات المغناطيسية الأرضية باستخدام جهازقياس المغناطيسية الأرضية (Overhauser magnetometer) وتحديد الإحداثيات والارتفاعات عن طريق جهاز (Global Positioning System GPS) . أظهرت قياسات التثاقلية والمغناطيسية ظهور عدد من الشاذات والتى تتمركز بالتوازى مع تمركز طبقات الحديد على السطح وتزيد مع التوجه نحو قمة الطية. أوضحت أيضا ظهور عدد من الصدوع ذات الاتجاهات شمال غرب - جنـــوب شـــرق وكـــذلك شرق-غرب.

تم استخدام طريقة (downward continuation) لتحديد أعماق الأجسام المسببة لهذه الشاذات حيث قدرت هذه الأعماق على أنها تتراوح مـــا بـــين ١٠٠-٤٠٠ متر. أما بالنسبة للدراسات المعدنية والجيوكيميائية فقد أظهرت أن نسبة الحديد في خام حديد أم نار قد تقارب نحو ٧٥% ممثلة غالبا بمعدن الماجنيتيت والهيماتيت أحيانا، كما أن توزيع العناصر الكيميائية المختلفة يرتبط بدرجة كبيرة باتجاه توزيع شرائط الخام .

ABSTRACT: *Banded Iron Formations (BIFs) have economic interest as they host the world's largest iron ore and much gold deposits. Umm Nar BIF is one of the oldest and biggest arc sedimentary rock units in the Precambrian sequence of the Eastern Desert of Egypt that strongly influenced by the deformation processes during or after the closure of the Mozambique Ocean (650-620 Ma). The result was multi-deformational phases of faults and folding. This study includes integrated geochemical and geophysical exploration methods. Detailed gravity and magnetic surveys were carried out in Umm Nar BIFs. Gravity method is suitable for detecting iron ores due to contrast density in compared to the schist country rocks. On the other hand, magnetic method is suitable for locating buried magnetite ore bodies. The detailed geological and geochemical studies were also carried out. Several reductions then filtering were done for both gravity and magnetic data. Obtained residual gravity and total intensity magnetic maps showed presence of high anomaly areas which are identical and compatible with the surface beds bearing the BIFs which reflects that the surface is extending subsurface mainly in the Northern Eastern part. The south-west high anomaly is compatible with the gabbroic pluton that invaded Umm Nar fold. Depth of the source body was estimated up to 350 meter using (Tikhonov et al., 1968) to regularize downward continuation to effectively help estimate the depths to the researched near surface gravity and magnetic sources. Geochemical analysis for collected surface samples showed high concentration of iron reaching up to 50-75% in the same areas of high gravity and magnetic anomaly.*

Key words: *Gravity, Magnetic, Downward continuation, Geochemical Analysis, Umm Nar Iron ore.*

INTRODUCTION

Mining in Egypt has had a long history that goes back to Predynastic times. Nevertheless, the scale of mining in Egypt at present is small. The largest mining operation which is of the iron ore does not exceed 3 million ton/year. Thus, the exploration and re-estimation of reserves of these ores are required. Drilling holes, then collecting subsurface samples and determining the chemical assay is extensively used in mineral

exploration. However, this way to determine the quantity and dimensions of the ore body, estimating its reserve, is so expensive and time-consuming.

Geophysical methods are capable of detecting and delineating local subsurface features of the ore body that could not be discovered by any realistic drilling program. Thus, the geophysical surveying can optimize exploration programs by maximizing the rate of ground coverage and minimizing the drilling requirement and reducing risks.

Integration of geophysical survey with geological and geochemical surveys is therefore of considerable benefits in exploration programs of ore deposits. Gravity and magnetic geophysical methods are passive potentials for exploration of subsurface iron ore deposits. Gravity is suitable for exploration of iron ores (e.g. Nabighian et al., 2005) due to its high density contrast with the country rocks, whereas the magnetic method is used (e.g. Mekkawi, 2012) because of their high magnetic susceptibility.

Iron ores in Egypt occur in two forms: ironstones and banded iron formations (BIFs). Ironstones were formed mainly within Phanerozoic sediments and are well represented in Bahariya and Aswan iron ores (e.g. Attia, 1950). Their mineralogical composition is mainly hematite in addition to goethite. On the other hand, BIFs occur in Precambrian island arc volcanic, volcaniclastic and sedimentary rocks. BIFs are composed mainly of magnetite, in addition to subordinate hematite. BIF mineralization was recorded in the Eastern Desert of Egypt in 13 localities between Safaga in the North and Marsa Alam in the South (Basta et al., 2011), and in South Western Desert in the area between Egyptian-Libyan border in the West to Gabal Kamel in the East and extends outside Egypt to the Libyan and Sudanese territories around Gabal Arkenu and around Gabal Kissu, respectively.

Umm Nar BIF is a good example to apply the integration between geological, geochemical and geophysical surveys for exploration of the iron ores in Egypt. It is one of the largest iron formation occurrences in Pan-African rocks in the Eastern Desert of Egypt. Based on the photo-geological and topographical maps of the deposit, Attia 1950 estimated its reserve as 15 million tons, whereas. El Ramly et al. 1963 made a preliminary estimation of the amount of the minable iron ore in the Umm Nar area as 8 million tons. Um Nar BIF is structurally complicated as affected by extensive folding and different faulting systems (El Aref et al., 1993a), and is intruded by igneous bodies of mafic dikes and granites. Detailed subsurface mapping and modeling over large sections of the Um Nar BIFs is lacking, complicating exploration and decreasing the chance to discover new occurrences of the deposits. Here we present a case study of Um Nar iron ore illustrating how the integration between geological, geochemical and geophysical (gravity and magnetic) data can be applied to ore exploration mapping and finding the relations between chemical elements anomalies and the ore-forming processes.

1. Geological setting and field occurrence of the Umm Nar BIF

The Neoproterozoic BIFs occur at thirteen localities in the Central Eastern Desert of Egypt (between latitudes 25 º 12□ and 26 º 40□ N) in island arc volcano-sedimentary assemblages (~750 Ma, Stern et al., 2004) of the Arabian Nubian Shield. This is consistent with their appearance on the Earth between 600-800 Ma (Klein, 2005; Ilyin, 2009). The island arc volcano-sedimentary assemblages attend to the opening of the Mozambique Ocean (Pearce, 2000; Stern et al., 2004). Oceanic volcanism and hydrothermal fluid circulation produced metalliferous and reducing ocean chemistry. Oxygen would react with ferrous iron dissolved in the sea water producing iron bands (e.g. Fortin and Langley, 2005; Salem and Hamdy, 2011).

Umm Nar deposit is the most southern one among the known BIFs in the Central Eastern Desert (between latitudes 25º 14□ 45□□ and 25º 16□ 18□□ N and longitudes 34º 15□ and 34º 17□ 27□□ E). The BIF in Um Nar area belongs to oxide and mixed silicate-oxide facies. Oxide facies bands are composed mainly of iron oxides mesobands alternating with chert mesobands. Mixed silicate-oxide facies comprises silicate laminae and batches within the iron bands. Comparing with the other BIFs, it is characterized by country rocks of metasediments (para-schist) formed in a back-arc sedimentary basin. They have good stratification and strong polyphase deformation of faulting and folding. Sedimentary rock units in Umm Nar enclosing the BIFs experienced polyphase modifications by regional, thermal and retrograde Pan-African-related metamorphism. Regional metamorphism is of low-pressure greenschist facies (El Habaak, 2004). However, rocks were locally affected by contact metamorphism (hornblende hornfels facies) (El Aref et al., 1993a; El Habaak, 2004) due to the small size of the intrusive body.

Umm Nar iron ore deposit lies near the upper part of Wadi Mubarak around Gabal El-Maiyit. It occurs within a series of schist belt (20 km long and as much as 6 km wide) (Fig. 1), representing the topmost part of the ophiolitic mélange. The schist belt ranges in composition from older hornblende and the actinolite schist, mica schist to younger graphite-chlorite schist. Iron bands occur usually within the mica schist (Fig. 2, A, B, C, D).

Umm Nar area is highly deformed. It was affected by two phases of regional deformation. The first phase resulted in a tight WNW–ESE striking and SW dipping overturned anticline plunging very steeply to the southeast (Loizenbauer et al., 2001). The iron bands have a lateral extension of about 8km, extending along strike of the Umm Nar anticline. They may sometimes also be contorted, discontinuous, turned and dislocated to the extent that they show no clear fold or cement pattern.

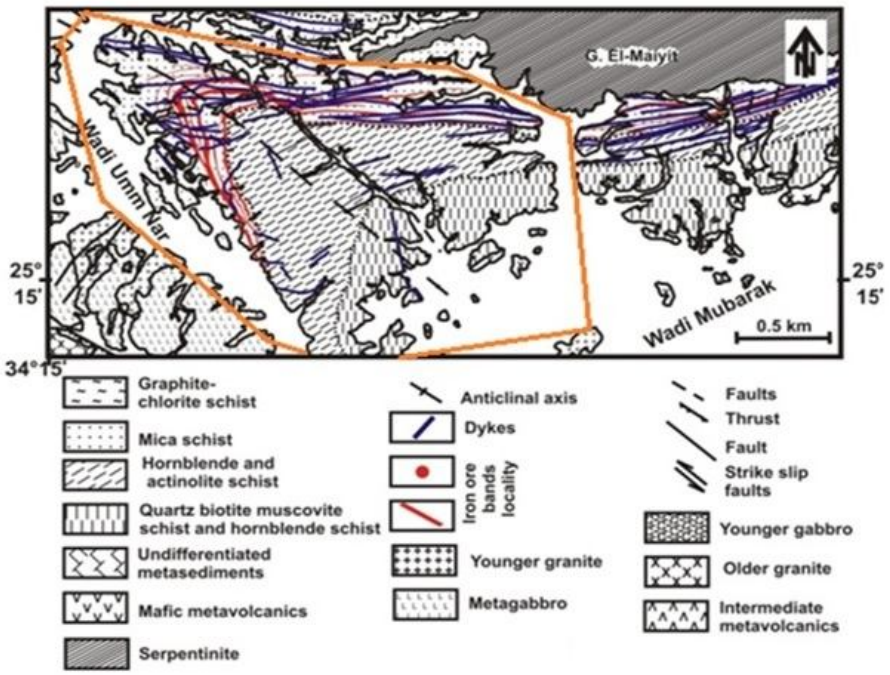

Fig. 1: Geological map of Umm Nar area (El Ramly et al., 1965), including the area of study.

Fig. 2: (A, B, C, D) Different locations of Umm Nar iron- Banded within the mica schist.

These folds which are usually about 1.5 meters across are clearly the result of compression of metasediments with their iron ore bands in the crest of the major fold. Confused fold structures are also cited with small nearly vertical dislocations and slip planes. Minor folds sometimes posse well-developed drag folds. First deformation phase also resulted in a series of E–W striking and south dipping thrusts that led to emplacement of the allochthonous sheets where iron bands run (~5 km) in the E-W direction parallel to the serpentinite mass of Gabal El-Maiyit and Wadi Mubarak. Second phase of the deformation produced a synform with an NW–SE trending and SE-plunging axis. The southwestern limb was interpreted to have been thrust onto the northeastern limb. In the southwestern limb, iron bands extend (~3 km) along the eastern side of Wadi Umm Nar and dip steeply to the S or SW at angles varying between 65º and 80º. Umm Nar BIF vary in thickness from few centimeters to a maximum of 5 m, but the majority does not exceed 1 m in thickness, attaining their maximum thickness at the conjugation of the fold limbs, but at either end they taper out and disappear.

Emplacement of the grey granites in the south-eastern corner of the area, as well as the huge masses of younger granites of Gabal Abu Diab, Gabal Umm Samra and Gabal Umm Bakra gave rise to considerable tectonic effecting, above all, the north-westerly shifting or displacement of huge anticline of the Umm Nar iron deposit. Accordingly, Umm Nar anticline which originally plunged moderately towards the South-East was made to stand with its axis nearly vertical and its axial plane running in a south-east direction and dipping steeply south-west to nearly vertical. Emplacement of the Younger Granite mass of Gabal Abu Diab in particular was accompanied by a thermal metamorphism superimposed upon the regionally metamorphosed metasediments with iron ore bands. In addition, hosting mica schist and sometimes hornblende schist are cut by massive intrusive mafic gabbroic dykes with slight local thermal effect in the South-West direction.

3. Methodology

3.1 Gravity survey

Gravity survey was applied in this study due to high density contrast between iron ore (3.8 to 4.2g/cm^3) and the country schist rocks (2.4 to 2.7 g/cm^3). Bulk density was measured in Soil and Rock Mechanics Lab of the Faculty of Engineering, Ain Shams University. Ground gravity surveywas conducted on an area of ~ 4×3 Km^{2}of the exposed schist-hosted BIF at Wadi Umm Nar area, using a Scintrex CG-5 gravimeter with resolution of 1 µGal. Gravity data were collected along 28 linear traverses at 15 to 25 stations each traverse (Figs.3 & 4), with a total number of 500. Station spacing ranged from 25 to 100m, depending on the changes in gravity measurements. Position and elevation of stations was determined using Trimble Differential Global Positioning System (GPS) receiver (Fig. 5).

Several adjustments, termed gravity reductions, to the raw gravity data were done to yield the gravity anomaly. First step in data reduction was to compensate for earth tides and instrument drift that result in time-dependent variations in measured raw gravity data. Effects of the earth's surface topography on the gravity measurements were removed. Topographic correction was an important in present study due to high rigid topography of Umm Nar area (Fig. 6). Distant part of the terrain correction which treated by global elevation model were performed using ASTER GDEM that has a resolution of 60m. Constructed digital elevation model shows that the two limbs of Umm Nar anticlinal structure constitute two discontinuous ridges varying in altitude from 600 meters above sea level to a maximum of 700 meters near the axis of the structure (Fig. 7**,** A&B). This is consistent with the elevations measured by (El Ramly et al. 1963). Local models (Fig. 8, A & B) displayed the average elevation of Wadi Umm Nar is about 550 meters above sea level whereas that of Wadi Mubarak is about 520 meters.

Measured gravity was significantly affected by elevation changes due to surface topography. In order to mark anomalies caused by subsurface geology, gravity variations resulting from station elevation differences and topographic effects were removed from the data. Values of terrains which were removed were ranging from 0.6 to maximum terrain value of 1.58 mGal using Toposk program for terrain correction.

Simple Bouguer anomaly values were obtained by applying different corrections to construct Complete Bouguer anomaly map of Umm Nar BIF area (Fig. 9). Bouguer anomaly map shows gravity highs (~-40mGal) in the Northern east and central parts of the studied area and gravity lows (~ -48 mGal) away from the anticlinal fold towards west and south parts. This high anomaly can be referred to deep seated structures, shallower structures and presence of subsurface iron ore deposits.

Gravity field recorded at the Earth's surface is the cumulative effect at different depth, at least above the Moho. It is, therefore, essential to separate observed gravity field devoted to different depth. In general, these field are regional devoted to the deep-seated sources and residual to shallow sources. In prospecting for ore deposits, the residual gravity field is more important as it is related to a small area and shallow sources. Lateral variations in gravity anomalies are linked to anomalous density distributions within the Earth.

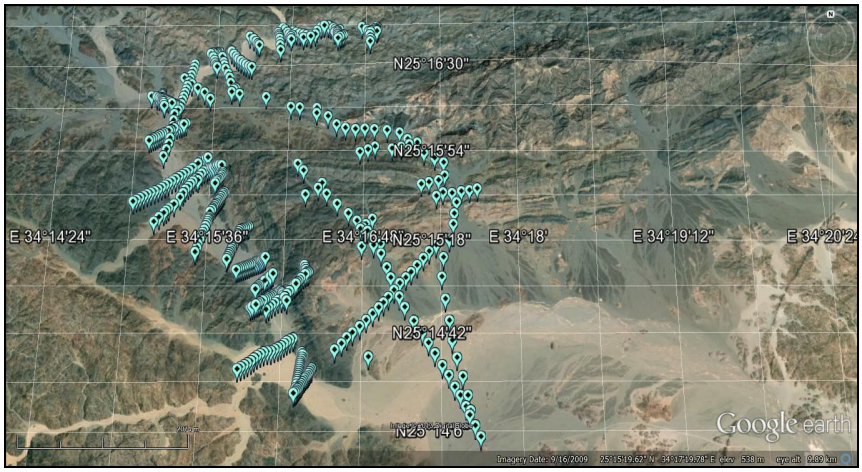

Fig. 3: Distribution of measured gravity points on Google earth map.

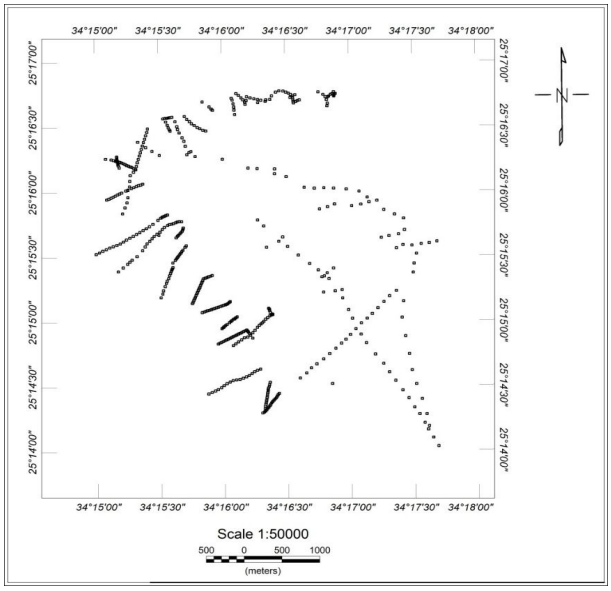

Fig. 4: Location map of the measured gravity points.

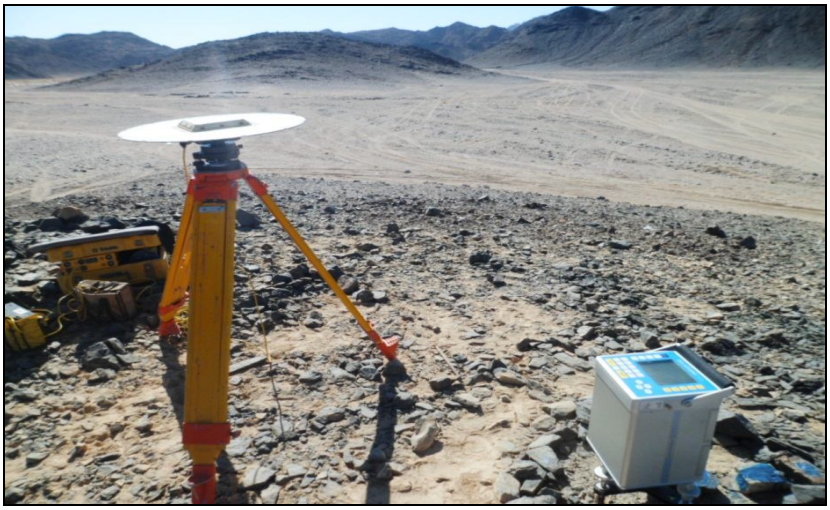

Fig. 5: Measuring gravity and detection the position using GPS at gravity base station.

Fig. 6: High rigid topography of Umm Nar BIF area.

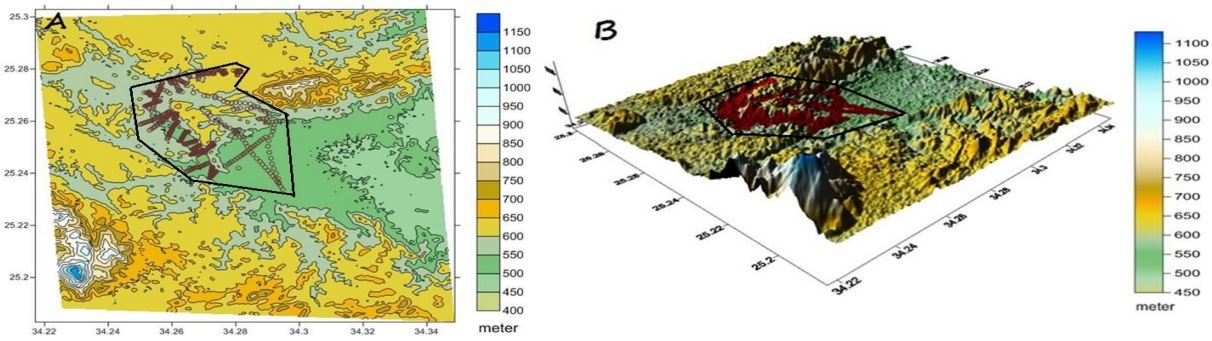

Fig. 7: (A, B) 2D & 3D ASTER Global Digital Elevation Model (ASTER GDEM) for Umm Nar BIF and surrounding area, respectively. The area of study is surrounded by red marks and the measured points around the anticline are shown.

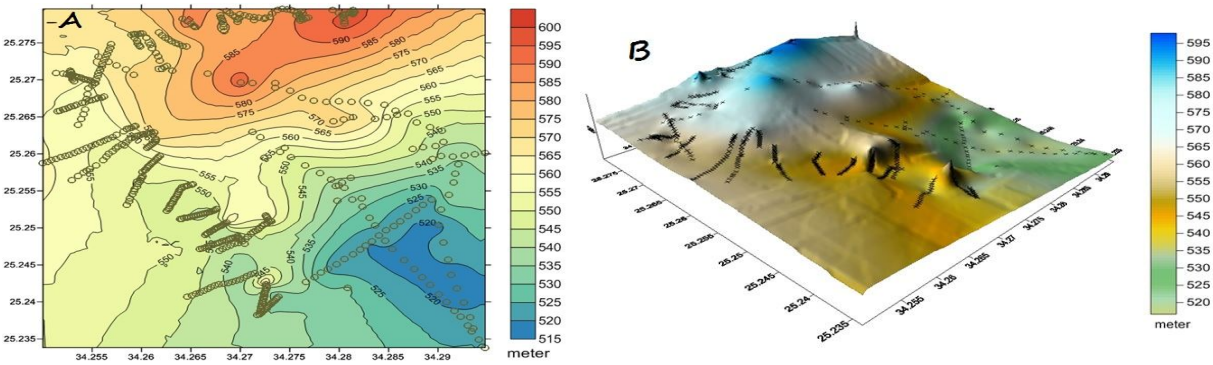

Fig. 8: (A, B) 2D & 3D local digital elevation model using measured points by Global Positioning System (GPS), respectively. Circles refer to GPS measurements.

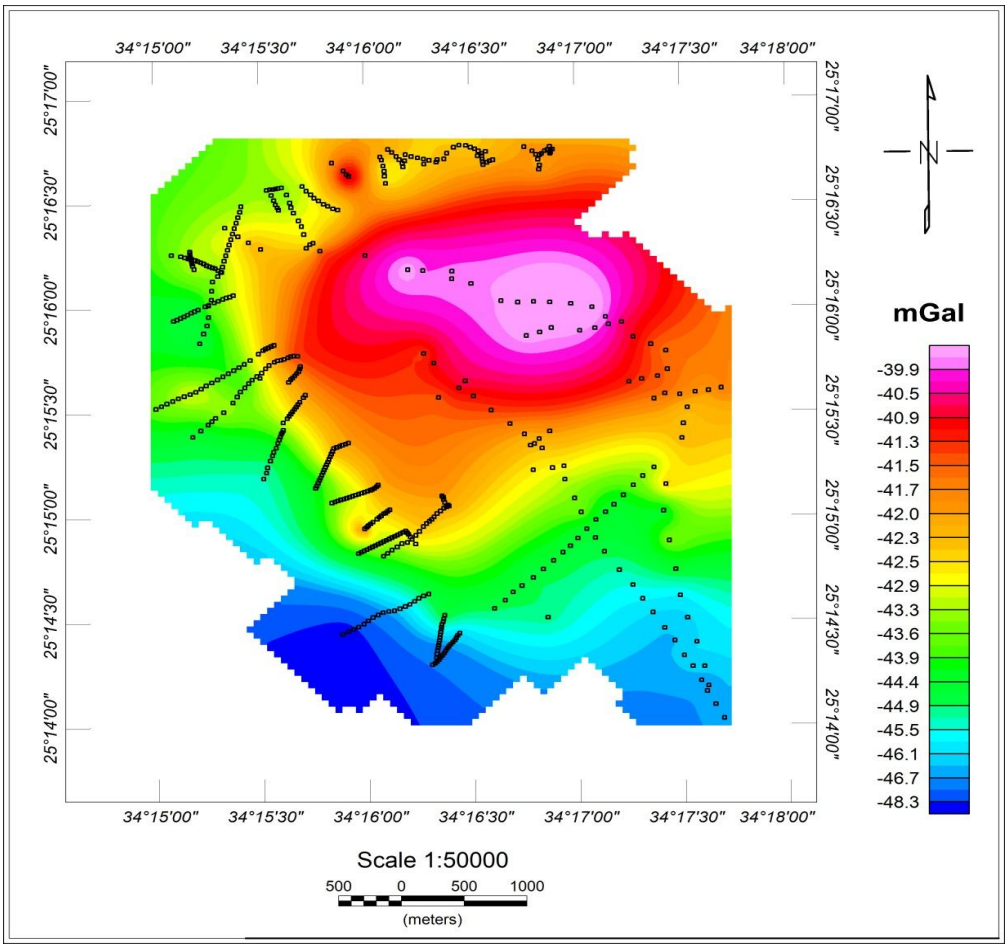

Fig. 9: Bouguer anomaly map of the Umm Nar area.

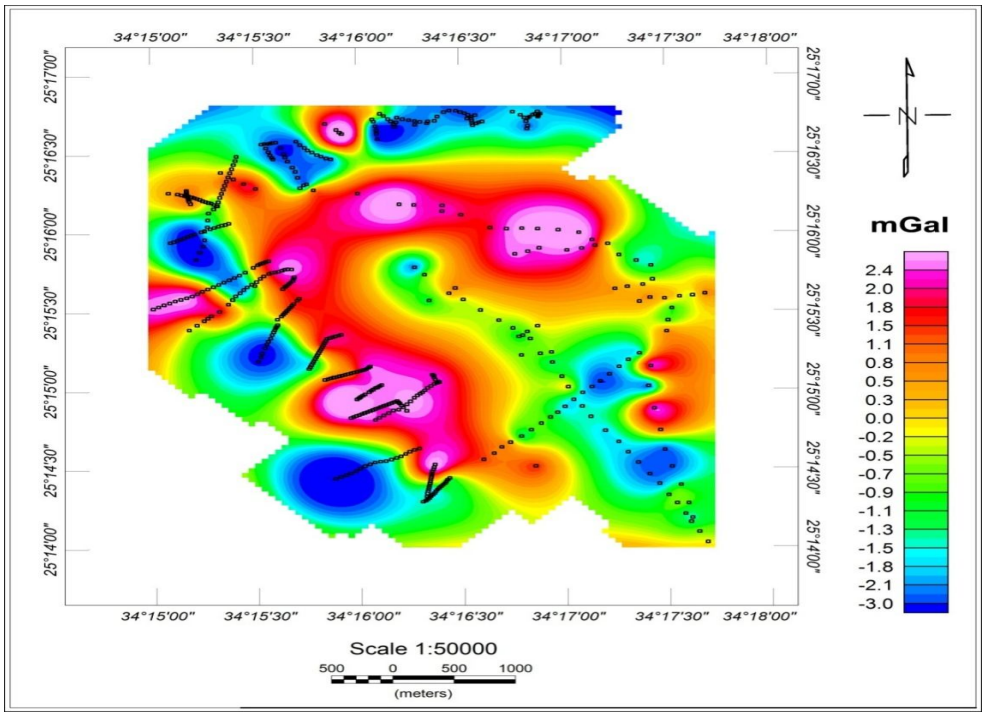

Fig. 10: Residual anomaly map of Umm Nar area.

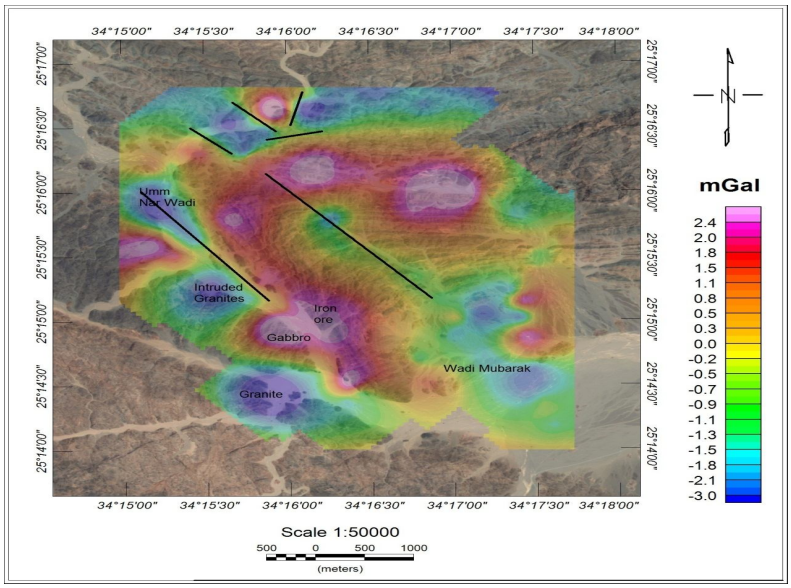

Fig. 11: Residual anomaly map of Umm Nar area based on Google earth map, illustrating some faults trending NW-SW, E-W & NE-SW.

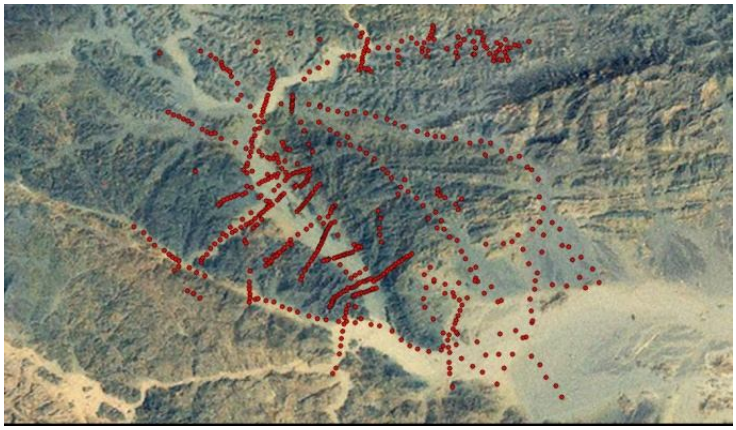

Fig. 12: Distribution of measured magnetic points on google earth map.

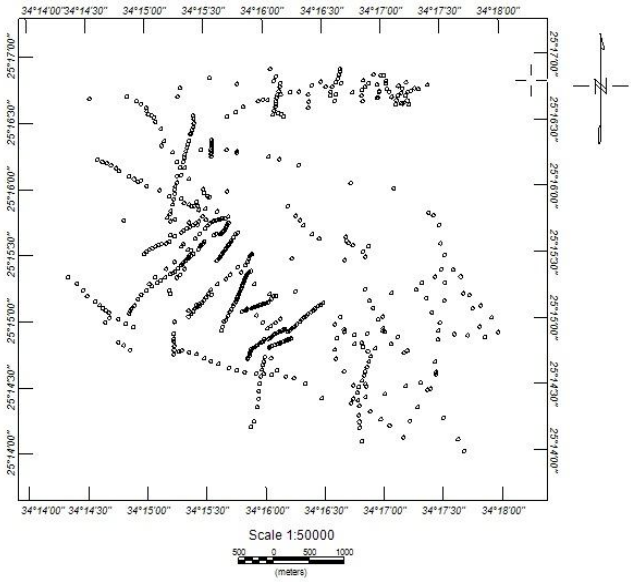

Fig. 13: Location map of the measured magnetic points.

In addition, the theoretical gravity (smoothed normal gravity) was removed leaving only local effects to produce the residual anomaly map of Umm Nar mineralizing area. To construct the residual anomaly map (Fig. 10 & Fig. 11), polynomial filter with trend order 2 was applied. Residual anomaly map shows gravity highs (~2.4 mGal) at scattered areas of Umm Nar BIF, concentrating mainly in the central part near the crest of the fold, also in north eastern part of the fold, and south western part of the fold. On the other hand, the gravity lows (~-3mGal) match the position of Wadi Mubarak at south and the distant western part of the fold, in addition, some scattered areas northern the fold.

From residual anomaly map, it is noticed that the south western high anomaly is related to the combined effect of gabbro pluton and bands of iron in the fold. Main high anomalies in the residual map are due to the effect of presence of iron bands which are mainly distributed near the axis of the fold and the north eastern part. In the other hand, the lowest anomaly in the south western part is related to the presence of granite. Wadi Mubarak also contains low anomalies which reveals to the termination of Umm Nar anticlinal fold that bearing iron bands and the effect of low density sediments increased. The fault system was deduced from the residual map. It includes three trends, NW-SE, E-W and NE-SW.

3.2 Magnetic survey:

Magnetic geophysical tool is effective due to high magnetic susceptibility of iron. The measured magnetic data for Umm Nar BIF were collected to cover 20 lines with 25 to 30 points collected along each line, for a total of 584 points with line spacing ranging from 25 to100 meters (Fig. 12 & Fig. 13) using both Proton-Precession and GSM-19 Overhauser magnetometers.

Values of measured magnetic points were corrected for the diurnal variations because the diurnal variation of the Earth's magnetic field may have amplitudes as great as 10 nT. This correction was applied daily in the field during the magnetic field.

After correcting the magnetic values for the diurnal variations, the total intensity magnetic map was produced (Fig. 14 and Fig. 15).

Shape of the magnetic anomaly varies dramatically with the dip of the earth's field, as well as with the changes in the shape of the source body and its direction of magnetization (Abu El-Ata, 2002). Total intensity magnetic map of the study area shows main high magnetic anomalies in eastern, central part and crest of Umm Nar anticline fold. These high magnetic anomalies are indication to the presence of subsurface iron ore of high magnetic susceptibility. South western part of the high anomaly is related to presence of the gabbro pluton. Adherence of the low magnetic intensity anomalies directly to those high ones without gradation may be due to the great difference between the values of magnetic intensity directly above iron in the mountain and readings in the Wadi. Generally, low magnetic intensity reflects presence of subsurface low magnetic susceptibility schist.

3.3 Depth Estimation of targeted anomalies:

Downward continuation of potential fields is a powerful, but very unstable tool used in the processing and interpretation of geophysical datasets. Treatment of the instability problem has been realized by various authors in different ways. Tikhonov (1968) regularization approach is one of the most robust. It is based on low-pass filter derivation in the Fourier spectral domain; by means of a minimization problem solution. Regcont Matlab code-based program (Pašteka et al., 2012) was used for applying downward continuation on gravimetry (Fig. 16) and magnetometry (Fig. 17) datasets. Optimum regularization parameter value is selected as a local minimum of constructed Lp-norms functions in the majority of cases; the C-norms give the best results. Main output of the proposed software solution is the estimation of the depth to source below the potential field measurement level (Pašteka et al., 2012).

Transformations of geophysical potential fields (mainly in gravimetry and magnetometry) play an important part during their processing and interpretation. Due to the harmonic property (fulfilling the Laplace equation), it is possible to realize the operation of analytical continuation of potential fields (upwards and downwards) in the source free domain. In the case, when gravity or magnetic data are continued further from the causative sources, it is considered to be upward continuation. On the contrary, when the causative sources locate below the measurement level (closer to the sources), it is considered downward continuation. Expected sources locate below the measurement level which is common situation in applied geophysics. This description of the operation is independent of orientation of vertical coordinate axis, which can be different depending upon the application (either pointing downwards or upwards) (Pašteka et al., 2012).

Data shows a very good ability of the regularization algorithm giving reliable results on levels close to the source position (a weak edge effect still occur, Figs. 16 and 17) for both gravity and magnetic data. From analysis of evaluated C-norms functions, it appeared that the vanishing of the local minimum in the C-norm functions occur at the depth 300 meter for gravity data and 350 meter for magnetic data which means that the causative body leading to these gravity and magnetic anomalies in Umm Nar area vanishes at depths 300, 350 meter, respectively.

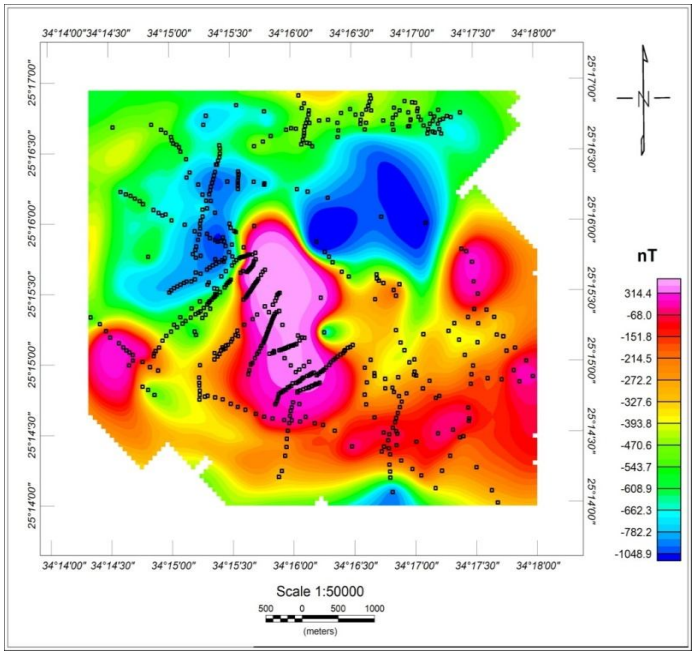

Fig. 14: Total intensity magnetic map of Umm Nar area.

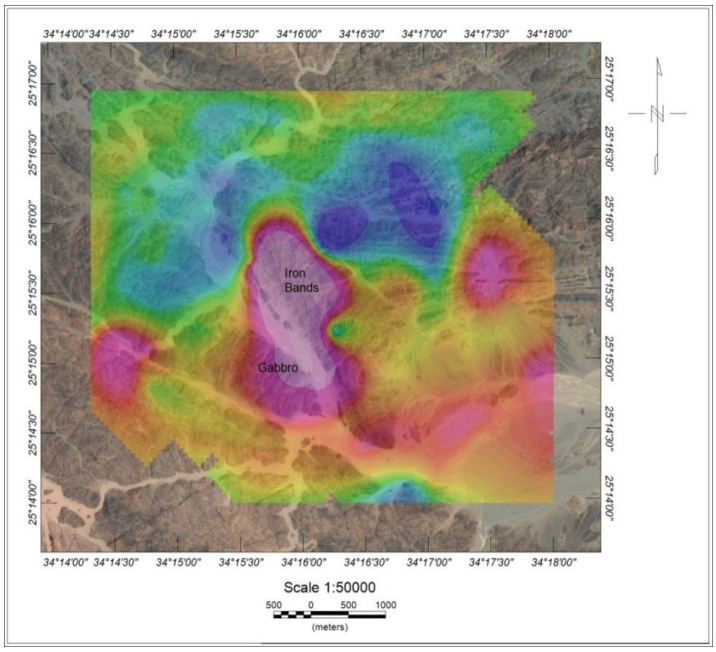

Fig. 15: Total intensity magnetic of Umm Nar area plotted on google earth map.

4. BIF Sampling and mineralogical and geochemical analysis

After detection of gravity and magnetic data anomalies, BIF samples were collected for mineralogical and geochemical perspective. Samples collected corresponding with geophysical anomalies of different degree of magnitude. The main aims of these mineralogical and geochemical analyses were to (1) correlate the mineralogical composition (particularly iron oxide minerals) with the geophysical anomalies, (2) statistically explore the data with respect to specific element associations and geochemical patterns by which the BIF samples can be grouped, (3) identify any geochemical anomalies that may present vectors to buried ore and (4) better characterize geological processes likely to cause variations in geochemical anomalies.

4.1 Mineralogy

Volumes of minerals (transparent and opaque) and textures of the iron ore were examined in about 20 thin polished sections, using a transmitting and reflecting light microscope. Mineralogy of the Umm Nar BIF was investigated using X-ray diffraction analysis. The most

abundant ferriferous minerals are magnetite, whereas hematite is the second in abundance. However, in some samples hematite is more abundant.Quartz, goethite, garnet, amphibole and calcite are subordinate. However, El Aref et al. (1993b) observed the stilpnomelane as a major ferriferous mineral in Umm Nar BIF. The iron ore sometimes contains minor amounts of sulphides (pyrite, chalcopyrite and covellite), epidote, graphite, and chlorite. On the basis of relative abundance of the iron ore minerals, three ore types are identified; including magnetite, magnetite- hematite and hematite ore types. However, the BIF in Umm Nar area belongs to the oxide and mixed silicate-oxide facies. Oxide facies bands are composed mainly of iron oxides mesobands alternating with chert mesobands. Mixed silicate-oxide facies comprises silicate laminae and batches within the iron bands (Fig. 18 C). It is worth noted that in general sites with higher magnetic anomaly appear to not usually contain more magnetite than hematite. This point to that the subsurface extension of the iron bands is mineralogically not usually similar to their surface exposure.

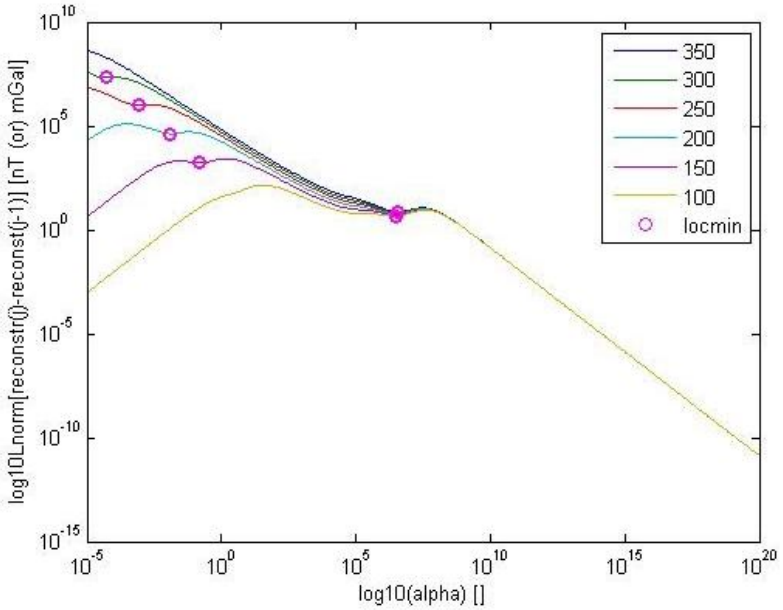

Fig. 16: C norms for the Downward Continuation of gravity data, with levels from 100 up to 350 meter with step value: 50 meter.

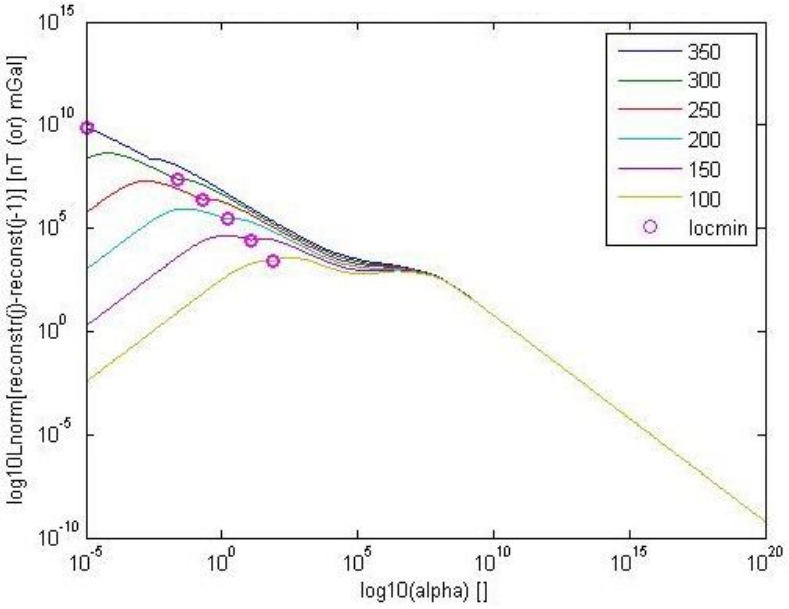

Fig. 17: C norms for Downward Continuation of magnetic data, with levels from 100 up to 350 meter with step value: 50 meter.

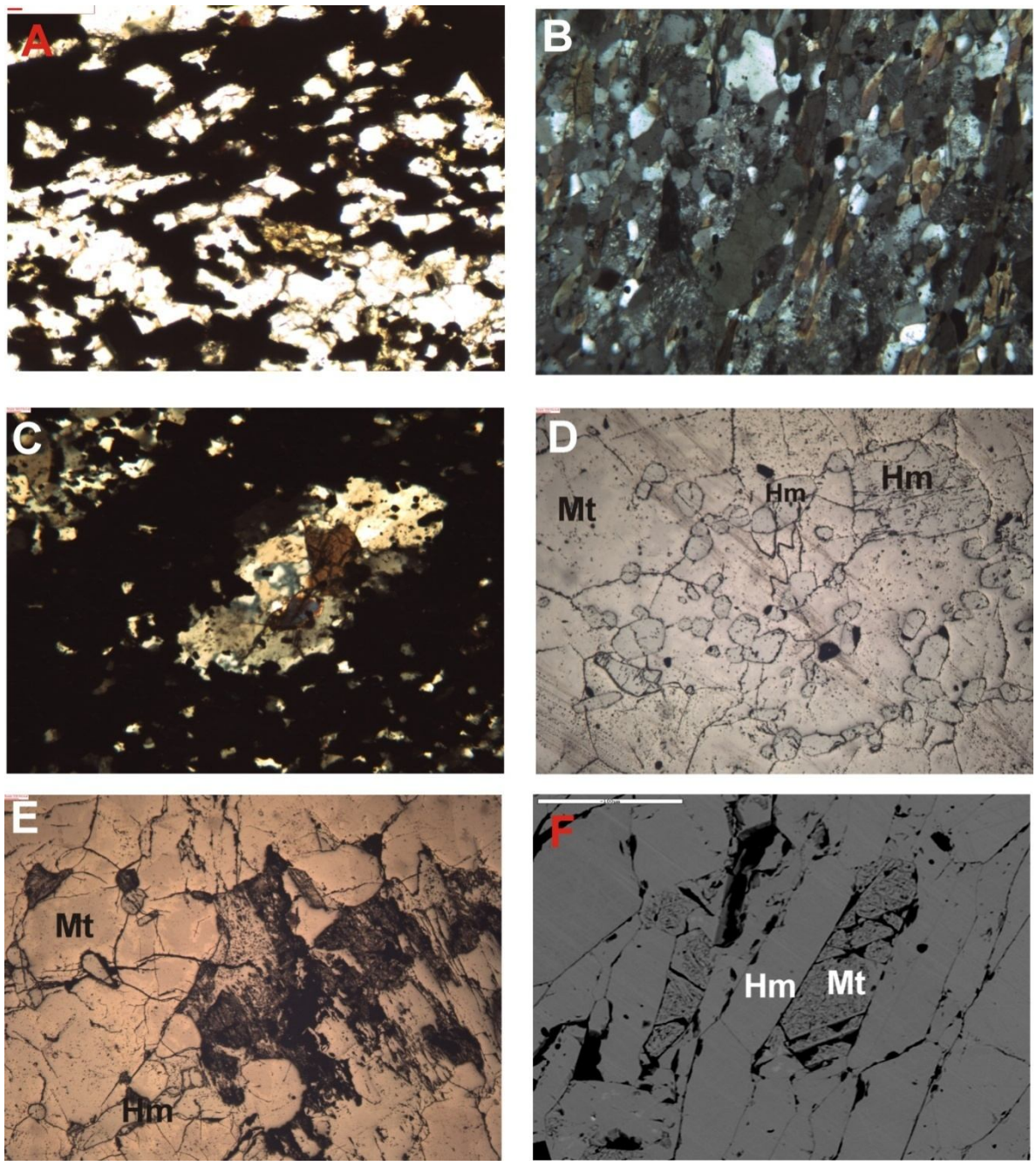
A
B
C
D
Mt
Hm
Hm
E
Mt
Hm
F
Hm
Mt

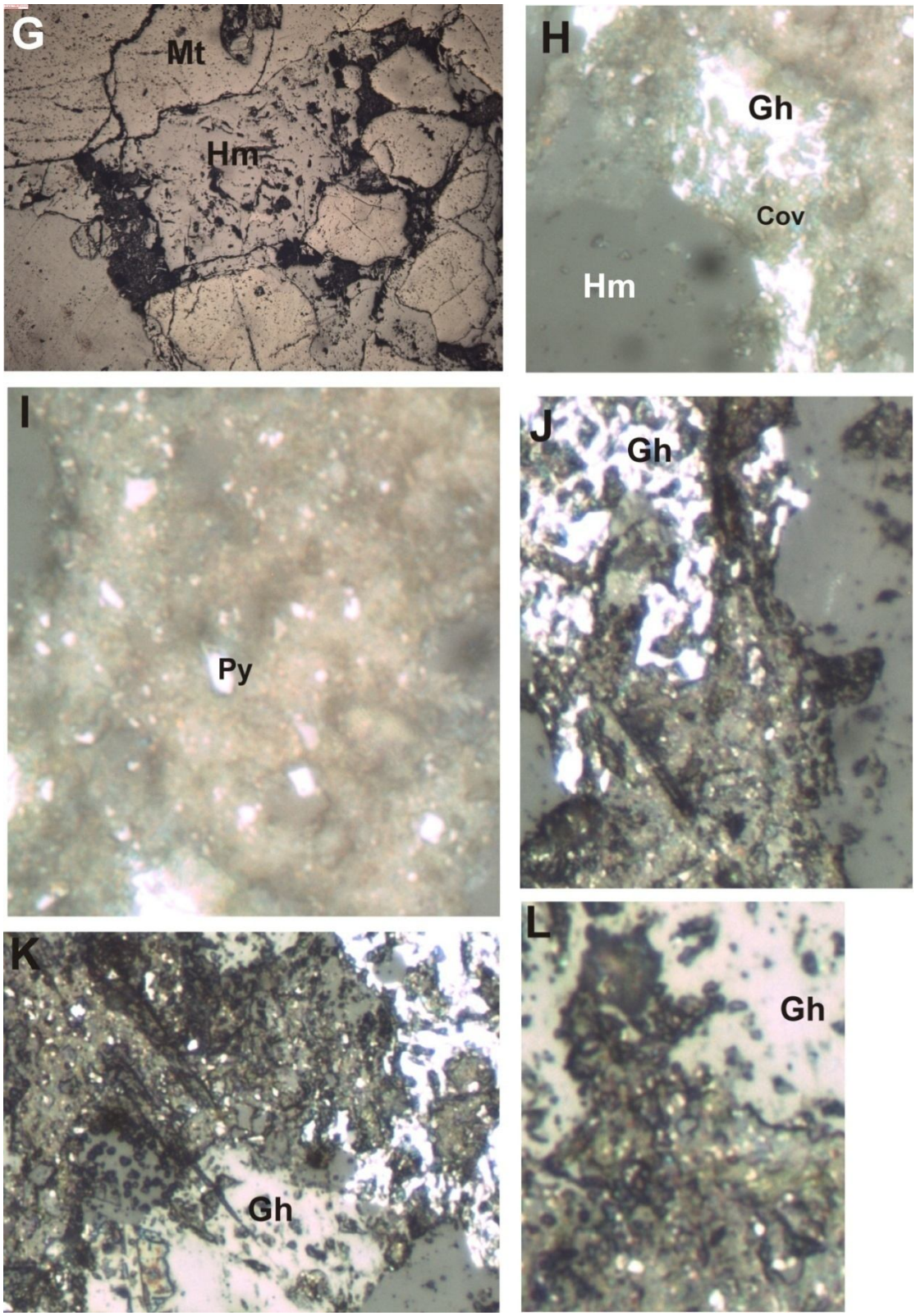
G
Mt
Hm
H
Gh
Cov
Hm
I
Py
J
Gh
K
Gh
L
Gh

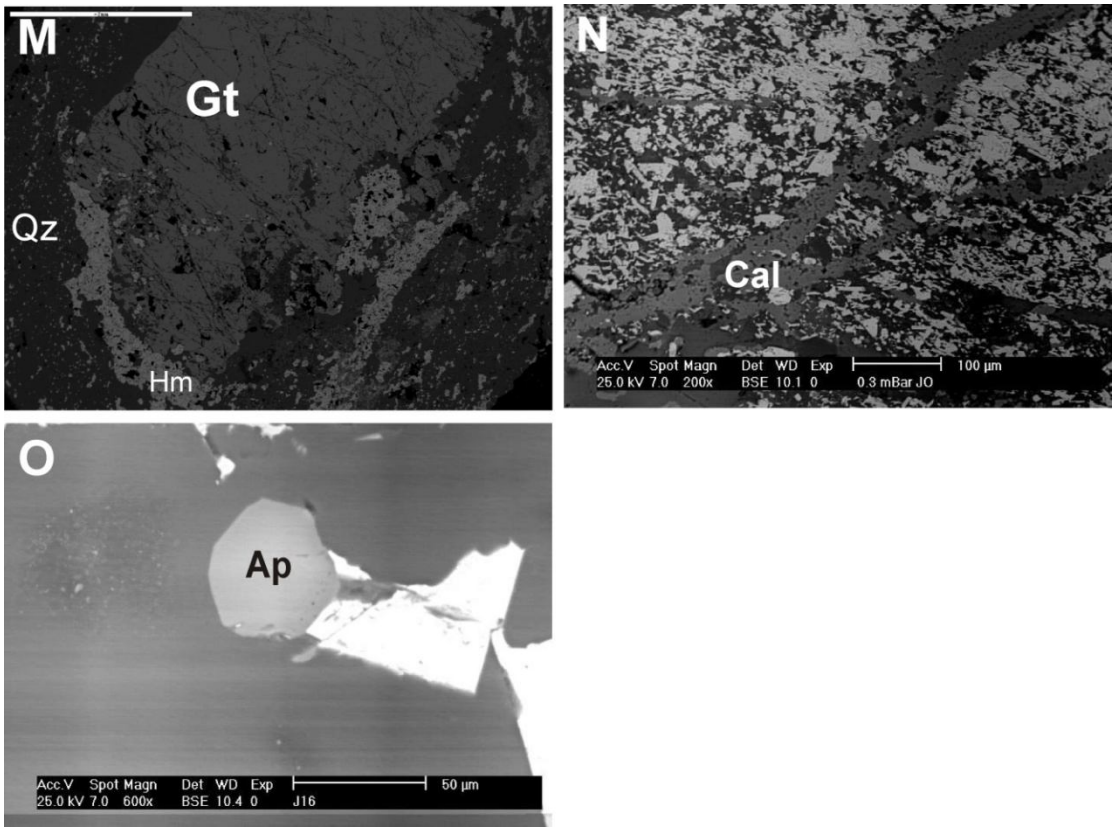

Fig. 18: A) Rhythmic alternation of BIF and silica rich macrobands, B) Salt and pepper texture in magnetite-hematite (Mt-Hm) bands with in the schist country rock, C) Silicate laminae and patches with in the iron mesobands, D) Salt and pepper texture of hematite (Hm) in magnetite (Mt) plates, E) Equi granulae magnetite (Mt) crystals enclosing ion hematite (Hm) and silicate patches. Magnetite (Mt) is variably martitized, F) Elongated magnetite (Mt) parallel to hematite (Hm) prisms displaying slight martitization, G) Magnetite (Mt) porphyroblasts in atoll-like structures, (H-L) Colloform and denderitic geothite (Gh) enclosing pyrite (Py) and covellite (Cov). M) BSEI(Back-cattered electron microscope) elongate garnet (Gt) porphyroblasts in quartz-rich (Qz) mesobands. It encloses inclusions of randomly oriented quartz grains forming sieve textures and obviously pushing aside hematite (Hm), N) calcite (Cal) laminea and veinlets cutting through Si- and Fe-rich bands, O) Subhedral discrette microcrystalline apatite (Ap) within silica band.

Elevated abundance of hematite and presence of gangue minerals in some samples may involve deposition, recrystallization, intergrowth, overgrowth, replacement and alteration (El Aref et al. 1993b). This can be interpreted from inspection of textures and interrelationships between minerals. Magnetite (few microns to 1.3 mm) forms either separate micro bands or is mixed with hematite. It also occurs disseminating that may represent residues of early formed magnetite, survived the subsequent deformation and metamorphic processes. Most of magnetite crystals display different degrees of martitization (formation of secondary hematite) (Figs. 18 D, E), which is most probably related to the near-surface oxidation of the studied samples. In some samples the magnetite crystals formed at the expense of hematite (Fig. 18. 1F).

In addition to martite, hematite occurs as euhedral crystals (70 to 250 µm long and 30 to 50 µm wide) oriented preferably parallel to rock foliation (Fig. 18.F), thus may indicate metamorphic recrystallization along bedding planes (e.g. James 1992). However, it occurs (5-10 µm) in salt and pepper texture among magnetite plates (Figs. 18.D, E) and survived the subsequent deformation and metamorphic processes. The sequential development of hematite and magnetite and magnetite pseudomorphs reveals that at least intermittent oxidation-reduction conditions prevailed during formation of the iron bands.

Goethite is a minor phase in Um Nar BIF. It is usually associated with sulphide minerals of pyrite and covellite and sometimes gold. This association may an indication for the oxidation and secondary growth processes (Figs. 18 H-L). Quartz in Fe-rich bands occurs interstitially among iron minerals, sieving magnetite and hematite inclusions. Calciteoccurs as subhedral to euhedral grains (0.03–0.07 mm) in thin laminae, augens or veinlets among Si- and Fe-rich bands (Fig. 18 N).Apatite is present usually with calcite

or in accumulation of anhedral grains (30–50 μm) or as in framboid structure of spherical aggregates (70–120 μm) of discrete equigranular euhedral microcrystallites, associating graphite (Salem and Hamdy, 2011). Graphite is present as irregular batches or as strands among the Fe-minerals or quartz grains. Figure 18 illustrates other several mineralization features and observations.

4.2 Whole-rock major and trace elements variations

Geochemistry oxides of Umm Nar deposit is systematically described (Table.1). The major oxide components are Fe_2O_3t (all iron as Fe^{3+} = 50.60-74.42%) and SiO_2 (12.52–43.55%). Fe_2O_3t is much higher and SiO_2 is much lower (except in samples# 11 and 17) than the iron-formations in other parts of the world of Klein (1993), whereas other oxides, except MgO and P_2O_5, are within this range. Contents of Fe_2O_3t and SiO_2 of Um Nar BIF have an inverse relationship to each other (r=-0.967). A remarkable feature is the high value of CaO (1.11-5.72%) that is reflected in high calcite contents in some samples.

Table 1: Chemical composition (major oxides in wt% and trace elements in ppm) of Umm Nar BIF ore types.

	Sample	Fe_2O_3t	Na_2O	MgO	Al_2O_3	SiO_2	P_2O_5	SO_3	K_2O	CaO	TiO_2	MnO	ZnO
Magnetite	2	74.42	1.01	1.51	3.83	12.52	3.04	0.02	0.351	3.03	0.141	0.041	0.004
	4	74.11	0.55	0.87	2.59	13.67	1.95	0.08	0.185	5.72	0.100	0.087	0.006
	5	69.53	0.53	0.84	2.33	22.11	1.95	0.04	0.183	2.26	0.100	0.036	0.005
	10	52.00	0.14	0.34	0.89	37.26	0.65	0.10	0.021	3.49	0.039	0.108	0.005
	11	49.21	0.12	0.46	1.12	42.29	0.92	0.08	0.024	2.97	0.041	0.133	0.006
	12	46.43	0.11	0.59	1.36	47.32	1.20	0.07	0.028	2.46	0.044	0.159	0.007
	15	70.84	0.07	0.47	1.89	19.71	0.76	0.12	0.018	5.87	0.096	0.085	0.006
	16	67.88	0.06	0.72	2.42	24.59	0.67	0.09	0.017	3.33	0.133	0.037	0.004
	17	48.52	0.12	0.50	1.18	43.55	0.99	0.08	0.025	2.84	0.042	0.140	0.006
	18	50.61	0.13	0.40	1.00	39.77	0.79	0.09	0.023	3.23	0.040	0.120	0.006
	20	74.26	0.78	1.19	3.21	13.09	2.49	0.05	0.268	4.38	0.121	0.064	0.005
	Average	61.62	0.33	0.72	1.98	28.72	1.40	0.07	0.104	3.60	0.081	0.092	0.005
Magnetite-hematite	3	70.13	0.07	0.39	1.14	22.32	0.84	0.08	0.024	4.76	0.079	0.081	0.007
	6	64.64	0.04	0.18	0.84	31.70	0.86	0.06	0.015	1.48	0.058	0.031	0.005
	7	63.71	0.11	0.15	0.67	31.31	0.52	0.09	0.016	3.17	0.048	0.049	0.005
	8	62.78	0.18	0.12	0.51	30.92	0.17	0.13	0.016	4.86	0.037	0.067	0.004
	14	61.99	0.05	0.40	1.39	32.13	0.56	0.07	0.015	3.23	0.079	0.044	0.005
	19	73.80	0.09	0.23	1.36	14.82	0.85	0.15	0.018	8.41	0.059	0.132	0.007
	Average	66.17	0.09	0.24	0.98	27.20	0.63	0.10	0.017	4.32	0.060	0.067	0.005
Hematite	1	66.45	0.06	0.56	0.91	29.83	0.83	0.02	0.029	1.11	0.099	0.030	0.007
	9	56.10	0.03	0.07	0.35	39.67	0.45	0.06	0.012	3.14	0.024	0.051	0.005
	13	63.96	0.05	0.11	0.42	29.13	0.85	0.06	0.055	1.22	0.014	0.017	0.006
	Average	62.17	0.05	0.24	0.56	32.88	0.71	0.04	0.032	1.82	0.046	0.033	0.006

	Sample	SrO	Cl	Pb	Zn	Cu	Ni	Co	Cr	V	Sc	Ga	Se
Magnetite	2	0.014	0.019	0.30	49.78	47.34	5.26	373.60	57.35	61.58	9.38	2.90	4.79
	4	0.013	0.031	3.67	68.45	45.64	3.13	342.63	59.26	48.98	13.32	2.34	3.87
	5	0.012	0.022	2.26	56.01	49.97	6.83	349.63	152.94	47.58	6.00	2.92	6.21
	10	0.011	0.096	4.87	65.19	104.99	0.14	263.79	80.11	51.98	5.50	17.83	4.76
	11	0.016	0.063	7.40	76.16	145.27	0.07	260.69	99.32	65.17	4.52	10.25	5.36
	12	0.020	0.030	9.93	87.12	185.55	0.00	257.59	118.53	78.37	3.55	2.68	5.97
	15	0.013	0.039	7.81	68.45	51.39	5.31	328.72	61.18	40.58	12.33	2.72	3.36
	16	0.013	0.036	8.59	49.78	58.85	9.63	345.79	61.18	44.78	7.40	3.67	3.76
	17	0.017	0.055	8.03	78.90	155.34	0.80	259.92	104.12	68.47	4.28	8.36	5.51
	18	0.014	0.079	6.14	70.68	125.13	0.61	262.24	89.72	58.58	5.01	14.04	5.06
	20	0.014	0.025	1.98	59.12	46.49	4.20	358.11	58.31	55.28	11.35	2.62	4.33
	Average	0.014	0.045	5.54	66.33	92.36	5.54	309.34	85.64	56.49	7.51	6.39	4.82
Magnetite-hematite	3	0.012	0.032	4.40	87.12	44.06	1.94	306.59	59.26	27.99	11.13	2.20	2.37
	6	0.009	0.024	4.23	62.23	52.60	0.40	325.67	248.53	33.59	2.62	2.94	7.63
	7	0.007	0.098	2.27	56.01	43.77	4.85	311.02	149.12	32.19	5.31	18.86	5.83
	8	0.004	0.171	0.31	49.78	34.93	1.30	296.37	49.71	30.79	8.01	34.77	4.04
	14	0.009	0.032	4.90	56.01	42.87	1.00	280.79	70.74	29.39	6.99	2.21	3.22
	19	0.012	0.042	7.03	87.12	43.93	0.99	311.66	61.18	36.39	17.26	1.77	2.96
	Average	0.009	0.066	3.86	66.38	43.69	9.75	305.35	106.42	31.72	8.55	10.46	4.34
Hematite	1	0.011	0.022	1.77	87.12	44.19	2.89	301.52	57.35	19.59	5.00	2.64	1.79
	9	0.004	0.027	1.21	62.23	26.88	2.36	215.78	80.29	13.99	6.58	0.75	2.69
	13	0.010	0.000	2.88	68.45	38.00	1.76	259.41	49.71	16.79	5.20	0.99	2.36
	Average	0.008	0.016	1.95	72.60	36.36	5.67	258.90	62.45	16.79	5.59	1.46	2.28

	Sample	As	Br	Rb	Sr	Y	Zr	Nb	Mo	Ag	Cd	Sb
Magnetite	2	3.53	0.96	8.77	1.30	3.09	8.27	0.26	0.96	18.38	0.17	4.74
	4	0.05	0.85	5.57	8.65	7.98	7.92	0.58	0.75	16.78	0.46	1.50
	5	1.31	0.30	5.20	0.65	5.47	8.73	0.88	0.08	17.54	0.22	7.60
	10	7.21	3.52	2.90	5.02	3.93	0.37	0.64	4.07	9.87	0.20	3.78
	11	4.94	9.30	3.86	88.90	4.74	4.23	4.88	1.80	9.23	0.10	41.82
	12	22.66	25.08	4.81	112.78	15.56	18.08	5.13	29.52	8.59	0.00	39.87
	15	35.46	2.42	1.84	38.00	22.96	14.00	6.77	2.22	16.15	1.51	61.14
	16	36.33	3.10	1.30	0.00	23.04	20.43	7.63	2.89	17.11	1.26	64.03
	17	24.37	20.74	4.10	94.87	14.95	15.19	4.94	23.73	9.07	0.08	41.33
	18	26.08	16.41	3.38	76.96	14.33	12.30	4.76	17.93	9.55	0.15	42.80
	20	48.79	1.91	7.17	109.97	45.54	23.09	6.92	1.85	17.58	1.32	63.12
	Average	35.88	9.87	4.44	78.83	26.51	17.51	6.04	10.89	13.62	0.95	52.89
Magnetite-hematite	3	29.39	2.05	1.92	73.89	11.44	14.49	6.37	1.58	14.81	1.68	56.77
	6	49.10	2.63	1.63	0.00	17.85	9.19	6.50	2.21	16.71	5.26	50.46
	7	41.79	2.98	1.45	11.88	15.77	6.45	5.56	1.12	14.42	2.85	51.27
	8	34.49	3.32	1.28	23.77	13.68	3.70	4.63	0.03	12.13	0.43	52.07
	14	30.34	2.43	1.14	11.72	14.91	12.23	6.22	2.67	13.26	1.17	51.53
	19	34.58	1.74	2.38	76.00	22.88	7.57	5.91	1.54	15.19	1.76	58.26
	Average	36.61	2.52	1.63	32.88	16.09	8.94	5.86	1.52	14.42	2.19	53.39
Hematite	1	24.20	2.35	1.47	71.79	0.00	21.41	6.84	1.62	14.43	1.61	55.28
	9	24.36	1.76	0.97	23.45	6.77	4.02	4.81	2.44	9.40	1.08	39.03
	13	34.80	2.46	0.89	65.38	19.17	12.27	4.80	1.61	11.67	0.00	45.43
	Average	27.78	2.19	1.11	53.54	8.65	12.57	5.49	1.89	11.83	0.89	46.58

	Sample	Ba	La	Ce	Nd	Ta	W	Hg	Tl	Pb	Bi
Magnetite	2	200.56	5.33	43.82	0.00	0.20	81.25	24.22	0.00	0.00	17.96
	4	113.59	6.30	36.37	0.00	0.10	68.44	12.11	8.27	3.52	16.18
	5	132.71	4.39	30.40	0.00	0.10	66.47	12.11	10.87	2.11	17.70
	10	52.20	3.97	7.81	2.36	15.77	25.67	76.54	14.57	4.87	10.00
	11	65.10	3.60	5.08	1.18	24.45	16.83	118.64	13.17	7.40	8.75
	12	78.01	3.22	2.34	0.00	33.12	7.99	160.74	11.78	9.93	7.50
	15	24.39	9.51	25.56	4.27	0.00	59.66	0.00	19.18	7.81	16.53
	16	22.18	11.76	22.21	8.53	0.00	63.69	0.00	21.84	8.59	18.65
	17	68.33	3.50	4.39	0.89	26.62	14.62	129.17	12.82	8.03	8.44
	18	58.65	3.79	6.45	1.77	20.11	21.25	97.59	13.87	6.14	9.37
	20	157.07	5.81	40.09	0.00	0.15	74.84	18.16	4.13	1.76	17.07
	Average	88.44	5.56	20.41	1.73	10.97	45.52	59.03	11.86	5.47	13.47
Magnetite-hematite	3	23.45	4.38	26.39	0.00	0.00	52.76	0.00	16.24	4.40	13.40
	6	64.86	3.45	16.98	0.00	0.00	51.70	0.00	21.74	4.23	17.45
	7	48.24	4.29	15.52	2.48	0.00	48.81	0.00	20.28	2.27	15.48
	8	31.62	5.13	14.07	4.96	0.00	45.91	0.00	18.82	0.31	13.50
	14	19.39	7.93	15.60	4.27	0.00	44.27	0.00	16.84	4.90	13.77
	19	26.61	7.27	28.92	0.00	0.00	55.62	0.00	16.53	7.03	14.41
	Average	35.69	5.41	19.58	1.95	0.00	49.84	0.00	18.41	3.86	14.67
Hematite	1	20.28	1.50	23.86	0.00	0.00	49.90	0.00	15.95	1.77	12.39
	9	16.60	4.10	8.98	0.00	0.00	24.84	0.00	11.84	1.21	8.90
	13	11.55	9.07	15.88	0.00	0.00	36.78	0.00	18.77	2.88	12.04
	Average	16.14	4.89	16.24	0.00	0.00	37.17	0.00	15.52	1.95	11.11

The Al_2O_3-SiO_2 discrimination diagram (after Wonder et al., 1988) (Fig. 19) shows that most of Umm Nar BIF plot in hydrothermal field and therefore primary chemical precipitation of Si + Fe might come mostly from hydrothermal input. However, three samples plot on the hydrogenous metalliferous side of the diagram, suggesting that precipitation of iron come from the sea water, by chemical reaction between oxygen in water and dissolved Si + Fe. The Fe/Ti–Al/(Al+Fe+Mn) diagram (Fig. 20) (after Bostrom, 1973) illustrates that Umm Nar BIF plots close to modern metalliferous hydrothermal sediments. Addition of Al_2O_3 to hydrothermal sediments decreases the Fe/Ti ratio and increases the Al content with respect to the hydrothermal elements, Fe and Mn. In addition, the high CaO / CaO + MgO (0.67 to 0.97) values in Umm Nar BIF were reported to be conspicuous in chemical sediments imprinted by hydrothermal fluids produced by basalt-seawater interaction close to the spreading ridge and active vents (Murray et al., 1991; Dasgupta et al., 1999). This was constrained by the stable isotope composition of carbonate minerals in Umm Nar BIF (Salem and Hamdy, 2011). The studied BIF are enriched with trace elements of P, Sb, As, W, Cu, Mo and Mn if compared with the mean oceanic crustal composition of Wedepohl and Hartmann (1994). These elements were mostly enriched as the result of hydrothermal fluids input into iron formations (Klein and Beukes, 1993; Manikyamba and Naqvi, 1995; Lottermoser and Ashley, 2000). The hydrothermal origin of Umm Nar BIF is in agreement with submarine magmatism and hydrothermal activity of Pan-African island arc assemblage (e.g., Sims and James, 1984; El Gaby et al., 1988; Hussein and El Sharkawi, 1990).

On the other hand, the strong positive correlations between Al_2O_3 on one side and TiO_2, MgO, Na_2O, K_2O, P_2O_5, Zr, Y, Rb and Ba in second hand is interpreted as a result of the incorporation of a detrital component contributed to the Umm Nar Fe-Si chemical precipitate (Ewers and Morris, 1981; Manikyamba et al., 1995).

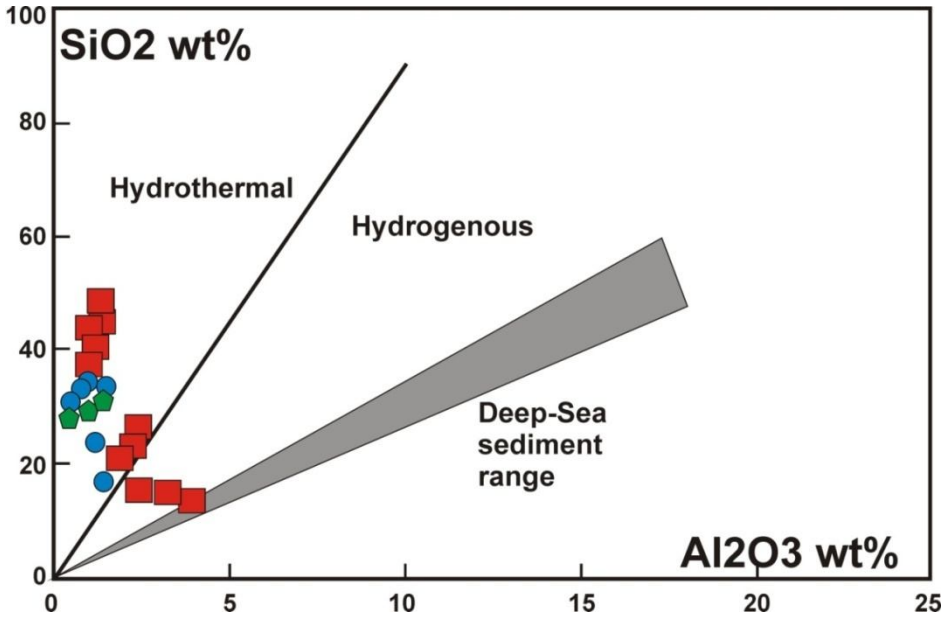

Fig. 19: Wonder et al. (1988) diagram which iliustrates the primary chemical precipetation of the Umm Nar BIF from hydrothermal solutions based on Al2O3-SiO2 contents.

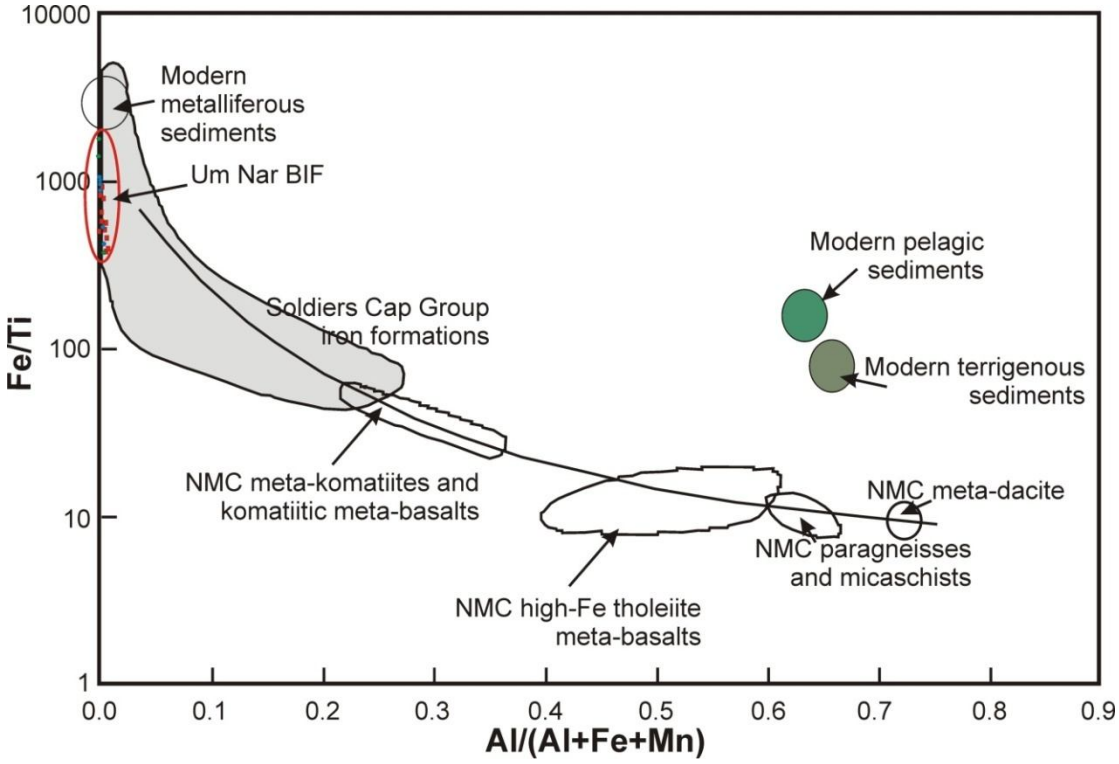

Fig. 20: Fe/Ti – Al/(Al+Fe+Mn) discrimination digram (after Bostrom,1973) showing the hydrothermal input and volcanic-clastic components in the hydrogenous sediment. The well known hydrothermal sediment of the Soldier cap Group iron formations (Hatton and Davidson, 2004) is plotted here (grey field) for comparison. NMC=Nogoli Metamorphic Complex.

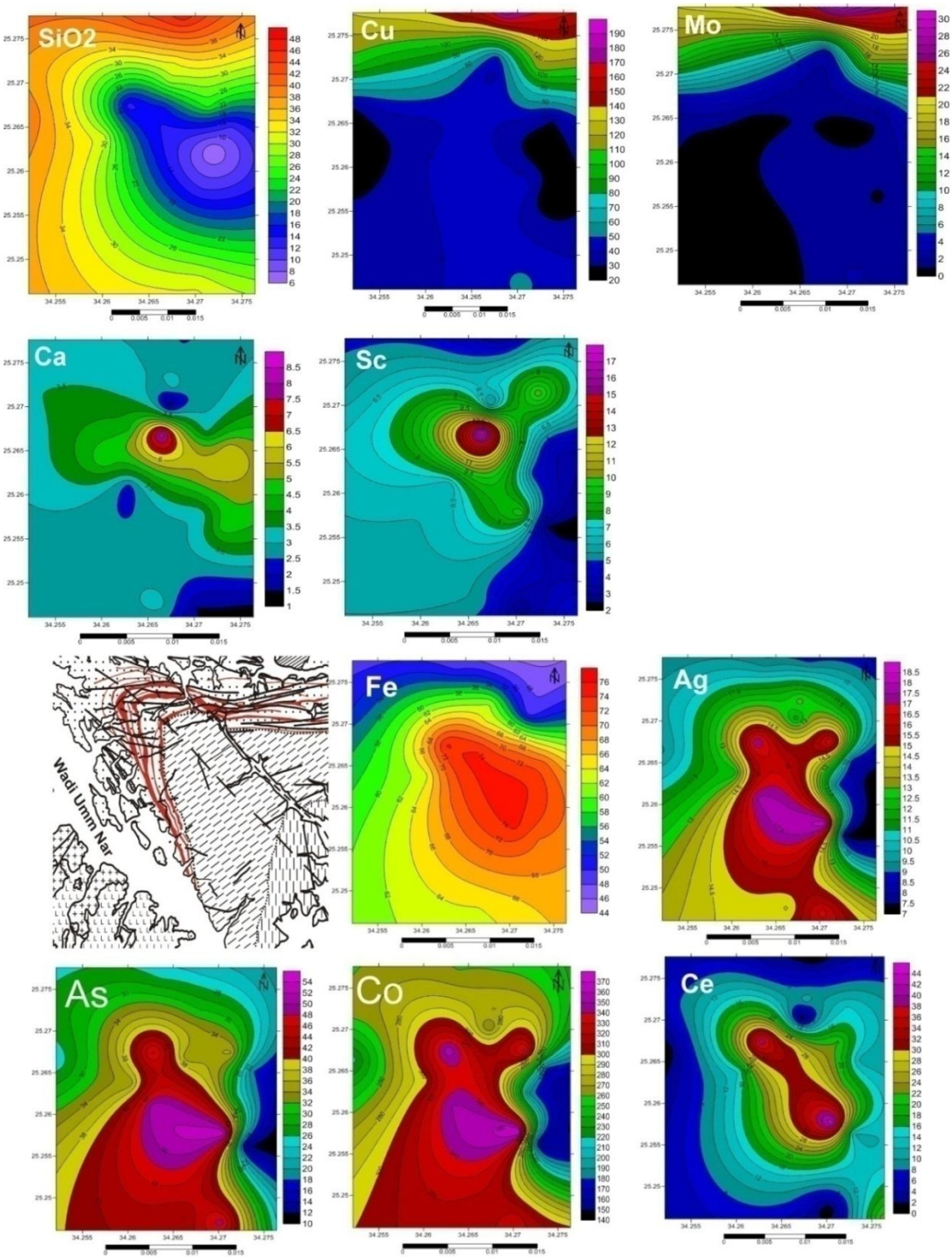

Fig. 21: Isochemical maps of some metals in Umm Nar BIF.

Additionally, Zr correlates with Al_2O_3 (r = 0.81) and TiO_2 (r = 0.78) (Fig.) that point to the admixture of a clastic "contaminant" to the chemical precipitate (Ewers and Morris, 1981).

4.2.1 Multi-element analysis:

When a geochemical prospecting survey is contemplated, geological factors likely to cause variations in primary geochemical halos expression of the target mineral deposit must be addressed. Elucidation of these factors in an orientation survey will permit the design of a geochemical prospecting survey that is most likely to prove effective under the prevailing conditions. The main types of primary halos are syngenetic and epigenetic. Syngeneic primary halos are formed essentially contemporaneously with the enclosing rocks. Epigenetic primary halos are formed after the host rock has solidified.

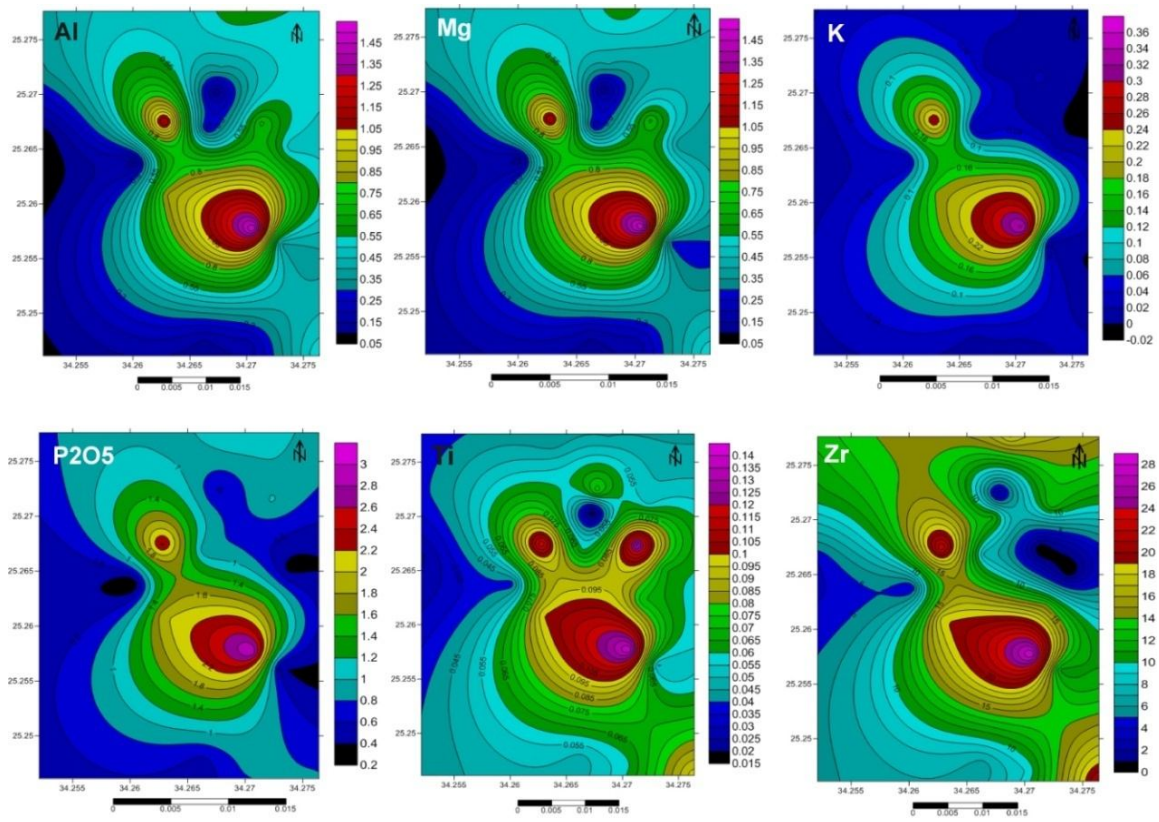

Fig. 21: Continuous.

We used the incompatible elements of LILEs and HFSE as pathfinders as they move further than other elements to offer the possibilities for successful discovery of other ores (such as gold). Statistical analysis is applied to major multielement surveys, including two dimensional representations of geochemical data involving automatic plotting and contouring procedures (geochemical mapping) and multivariate statistics where correlations between, and associations of, several elements are sought and distinguished.

4.2.1.1) Geochemical mapping:

Geochemical mapping is a common practice in the mineral exploration industry (McClenaghan et al 1997; Harris et al 2000; Adams 2006). Typically, metal concentration values were interpolated to create maps of one particular metal of interest (Fig. 21), which were used to delineate target areas for further exploration. This study exploits the fact that (i) the metal distribution in the Umm Nar BIF can be controlled by existing structural features and (ii) metals can be re-mobilized or introduced to the BIF due to post-mineralization events, resulting in a redistribution of elements and the creation of dispersion patterns along structural elements. Significance of geochemical maps will be discussed in combination with the multivariate statistics.

4.2.1.2) Element associations:

The Pearson linear correlation matrices (Table 2) are used to evaluate the interrelationships among the chemical elements in Umm Nar BIF (Fig. 22). These relationships divide elements into six associations:

i) Fe, Co, Ni, Ag, Nb, Sb, I, Ce, W, As

ii) Si

iii) Na, Al, Mg, P, K, Rb, Y, Ba, Ti, Zr

iv) Mn, Cu, Mo, V, Sr, Br ± Pb

v) Ca, Sc

vi) Cr, Se

***i)* Fe, Co, Ni, Ag, Nb, Sb, I, Ce, W, As**

The components of Co, Ni, Ag, Nb, Sb, I, Ce, W and As elements association together are strong indicator of iron ore (ore-controlled). In this association Ni, Co, As, Sb and Ag can be attributed to sulfide micro-aggregates of these elements. Meanwhile, the reason for strong loading of Ag in this factor may reflect that it is expected to find a significant amount of gold at Um Nar BIF. This is supported by values of high recorded Hg in surface samples.

Despite their high correlations with Fe, aureoles of all elements in the association, except Ce, are deviated from the NW-SE iron aureole trend to the WNW-ESE direction. This can be interpreted to represent a pervasive hydrothermal sulfidation (mainly arsenopyrite) of the Fe-rich bands of the BIF. This hydrothermal alteration might result from early structural modifications imposed by major transcurrent and thrusts faults (El Aref et al., 1993a), comprising the WNW-ESE shear zones.

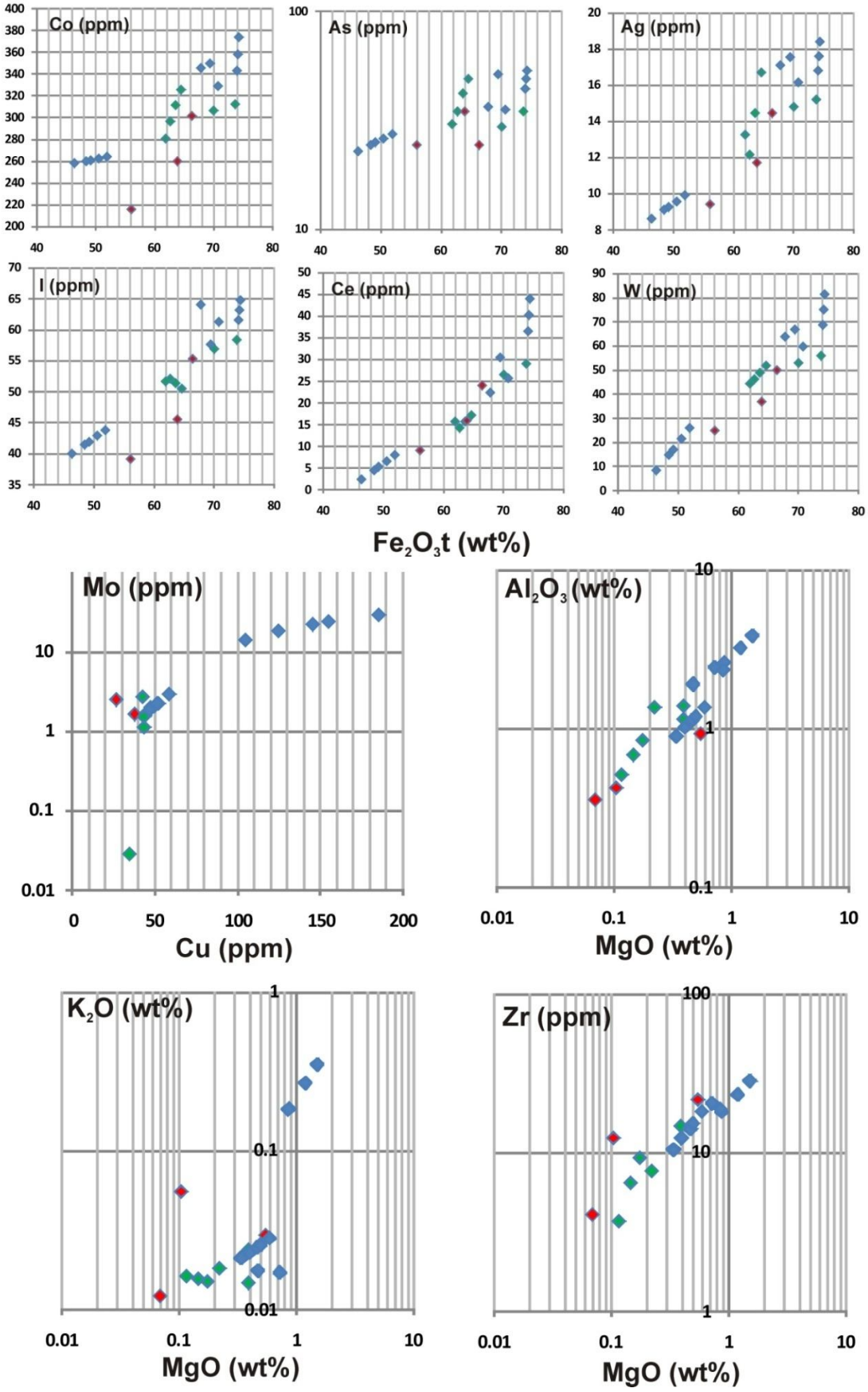

Fig. 22: Interrelationships among the chemical elements in Um Nar BIF.

Table (2): Pearson correlation coefficients of major and trace elements (Transform Log 10) in Um Nar BIF.

	Fe_2O_3t	Na_2O	MgO	Al_2O3	SiO_2	P_2O_5	SO_3	K_2O	CaO	TiO_2	V_2O_5	Cr_2O_3	MnO	ZnO
Fe2O3tot	1.00	0.48	0.40	0.56	-0.97	0.45	-0.09	0.52	0.41	0.70	-0.37	-0.23	-0.55	-0.21
Na2O	0.48	1.00	0.88	0.85	-0.61	0.94	-0.45	0.99	0.09	0.63	0.39	-0.15	-0.16	-0.07
MgO	0.40	0.88	1.00	0.95	-0.53	0.94	-0.50	0.89	0.01	0.82	0.54	-0.21	-0.07	0.14
Al2O3	0.56	0.85	0.95	1.00	-0.68	0.87	-0.32	0.85	0.21	0.87	0.46	-0.20	-0.10	0.07
SiO2	-0.97	-0.61	-0.53	-0.68	1.00	-0.57	0.04	-0.64	-0.51	-0.72	0.19	0.32	0.40	0.11
P2O5	0.45	0.94	0.91	0.87	-0.57	1.00	-0.56	0.97	0.01	0.64	0.46	-0.06	-0.09	-0.03
SO3	-0.09	-0.44	-0.50	-0.32	0.04	-0.56	1.00	-0.52	0.73	-0.34	-0.01	-0.18	0.49	0.25
K2O	0.53	0.99	0.89	0.85	-0.64	0.97	-0.52	1.00	0.02	0.64	0.32	-0.15	-0.23	-0.13
CaO	0.41	0.09	0.01	0.21	-0.51	0.01	0.73	0.02	1.00	0.15	0.031	-0.41	0.40	0.45
TiO2	0.70	0.63	0.82	0.87	-0.72	0.64	-0.34	0.64	0.15	1.00	0.16	-0.20	-0.34	0.09
V2O5	-0.30	0.39	0.55	0.48	0.12	0.45	0.05	0.32	0.09	0.23	1.00	0.15	0.67	0.37
Cr2O3	-0.23	-0.15	-0.21	-0.20	0.32	-0.06	-0.18	-0.15	-0.41	-0.20	0.12	1.00	-0.06	-0.49
MnO	-0.55	-0.16	-0.07	-0.10	0.40	-0.09	0.49	-0.23	0.40	-0.34	0.68	-0.06	1.00	0.69
ZnO	-0.21	-0.07	0.14	0.07	0.11	-0.03	0.25	-0.13	0.45	0.09	0.34	-0.49	0.69	1.00
SrO	-0.24	0.23	0.52	0.44	0.09	0.45	-0.14	0.25	-0.02	0.24	0.83	-0.03	0.61	0.44
Cl	-0.32	-0.19	-0.37	-0.37	0.29	-0.46	0.63	-0.32	0.23	-0.38	0.07	-0.04	0.27	0.08
Sc	0.71	0.31	0.25	0.44	-0.79	0.27	0.42	0.30	0.90	0.41	-0.12	-0.54	0.10	0.35
Co	0.82	0.66	0.68	0.79	-0.84	0.64	-0.16	0.67	0.24	0.86	0.11	0.02	-0.38	-0.21
Ni	0.68	0.17	0.14	0.27	-0.61	0.06	-0.08	0.21	0.27	0.47	-0.64	-0.54	-0.65	-0.09
Cu	-0.80	-0.16	0.03	-0.11	0.69	-0.04	0.07	-0.21	-0.21	-0.33	0.8	0.20	0.79	0.40
Ga	-0.32	-0.12	-0.33	-0.37	0.30	-0.39	0.49	-0.25	0.08	-0.38	0.06	-0.01	0.16	-0.06
Se	-0.33	0.19	0.13	0.11	0.29	0.21	-0.08	0.13	-0.28	-0.09	0.60	0.82	0.22	-0.35
As	0.72	0.71	0.52	0.64	-0.73	0.66	-0.27	0.72	0.07	0.57	0.01	0.27	-0.52	-0.60
Br	-0.87	-0.21	-0.06	-0.21	0.76	-0.12	0.10	-0.26	-0.22	-0.44	0.74	0.17	0.79	0.40
Rb	0.17	0.90	0.8	0.80	-0.34	0.93	-0.40	0.88	0.06	0.49	0.71	-0.05	0.23	0.16
Sr	-0.05	0.56	0.59	0.44	-0.13	0.67	-0.27	0.57	0.10	0.15	0.62	-0.31	0.50	0.48
Y	0.58	0.91	0.81	0.90	-0.71	0.89	-0.24	0.91	0.24	0.65	0.40	-0.09	-0.15	-0.22
Zr	0.14	0.71	0.71	0.52	-0.24	0.82	-0.65	0.74	-0.24	0.35	0.47	-0.03	0.08	0.16
Nb	0.77	0.45	0.64	0.74	-0.73	0.52	-0.36	0.50	0.09	0.94	-0.05	-0.02	-0.48	-0.07
Mo	-0.85	-0.19	-0.02	-0.17	0.74	-0.07	0.06	-0.23	-0.22	-0.40	0.75	0.17	0.79	0.42
Ag	0.93	0.54	0.54	0.68	-0.89	0.53	-0.21	0.58	0.23	0.83	-0.18	0.03	-0.57	-0.31
Cd	0.49	0.06	-0.02	0.09	-0.35	0.10	-0.19	0.08	-0.07	0.29	-0.32	0.70	-0.49	-0.50
Sb	0.81	0.09	0.13	0.33	-0.70	0.15	-0.14	0.16	0.17	0.57	-0.50	0.14	-0.63	-0.36
I	0.92	0.54	0.59	0.74	-0.93	0.50	-0.05	0.56	0.41	0.88	-0.10	-0.27	-0.42	-0.06
Ba	0.26	0.94	0.85	0.79	-0.40	0.94	-0.48	0.92	-0.05	0.52	0.59	0.12	0.01	-0.09
La	0.20	-0.31	-0.08	0.10	-0.22	-0.21	0.38	-0.25	0.32	0.15	-0.09	-0.40	0.03	0.04
Ce	0.83	0.71	0.74	0.81	-0.90	0.67	-0.11	0.71	0.50	0.85	-0.11	-0.46	-0.19	0.23
W	0.96	0.62	0.56	0.70	-0.94	0.56	-0.18	0.65	0.30	0.82	-0.22	-0.15	-0.59	-0.26
Tl	-0.13	-0.86	-0.79	-0.67	0.29	-0.86	0.49	-0.84	-0.04	-0.38	-0.49	0.24	-0.15	-0.26
Pb	-0.44	-0.47	-0.14	-0.08	0.37	0.29	0.42	-0.48	0.17	-0.13	0.50	0.08	0.67	0.40
Bi	0.87	0.47	0.44	0.62	-0.83	0.42	-0.11	0.50	0.21	0.75	-0.20	0.09	-0.62	-0.45
Ni+Co+Cu	0.09	0.51	0.74	0.72	-0.22	0.60	-0.10	0.48	0.07	0.60	0.83	0.11	0.34	0.21
CaO+MgO	0.48	0.27	0.22	0.41	-0.60	0.20	0.61	0.21	0.98	0.31	0.14	-0.44	0.37	0.47

	ZnO	**SrO**	**Cl**	**Sc**	**Co**	**Ni**	**Cu**	**Ga**	**Se**	**As**	**Br**	**Rb**	**Sr**	**Y**	**Zr**	**Nb**	**Mo**
Fe2O3t	-0.21	-0.24	-0.32	0.71	0.82	0.68	-0.80	-0.32	-0.33	0.72	-0.87	0.17	-0.05	0.58	0.14	0.77	-0.85
Na2O	-0.07	0.23	-0.19	0.31	0.66	0.17	-0.16	-0.12	0.19	0.71	-0.21	0.90	0.56	0.91	0.71	0.45	-0.19
MgO	0.14	0.52	-0.37	0.25	0.68	0.14	0.03	-0.33	0.13	0.52	-0.06	0.88	0.59	0.81	0.71	0.64	-0.02
Al2O3	0.07	0.44	-0.37	0.44	0.79	0.27	-0.11	-0.37	0.11	0.64	-0.21	0.80	0.44	0.90	0.52	0.74	-0.17
SiO2	0.11	0.09	0.29	-0.79	-0.84	-0.61	0.69	0.30	0.29	-0.73	0.76	-0.34	-0.13	-0.71	-0.24	-0.73	0.74
P2O5	-0.03	0.45	-0.46	0.27	0.64	0.06	-0.04	-0.39	0.21	0.66	-0.12	0.93	0.67	0.89	0.82	0.52	-0.07
SO3	0.25	-0.14	0.63	0.42	-0.16	-0.08	0.07	0.49	-0.08	-0.27	0.10	-0.40	-0.27	-0.24	-0.65	-0.36	0.06
K2O	-0.13	0.25	-0.32	0.30	0.67	0.21	-0.21	-0.25	0.13	0.72	-0.26	0.88	0.57	0.91	0.74	0.50	-0.23
CaO	0.45	-0.02	0.23	0.90	0.24	0.27	-0.21	0.08	-0.28	0.07	-0.22	0.06	0.10	0.24	-0.24	0.09	-0.22
TiO2	0.09	0.24	-0.38	0.41	0.86	0.47	-0.33	-0.38	-0.09	0.57	-0.44	0.49	0.15	0.65	0.35	0.94	-0.40
V2O5	0.37	0.80	0.13	-0.06	0.21	-0.63	0.75	0.11	0.61	0.05	0.68	0.70	0.58	0.39	0.44	0.04	0.69
Cr2O3	-0.49	-0.03	-0.04	-0.54	0.02	-0.54	0.20	0.00	0.82	0.27	0.17	-0.05	-0.31	-0.09	-0.03	-0.02	0.17
MnO	0.69	0.61	0.27	0.10	-0.38	-0.65	0.79	0.16	0.22	-0.52	0.79	0.23	0.50	-0.15	0.08	-0.48	0.79
ZnO	1.00	0.44	0.08	0.35	-0.21	-0.09	0.40	-0.06	-0.35	-0.60	0.40	0.16	0.48	0.22	0.16	-0.07	0.42
SrO	0.44	1.00	-0.34	-0.02	0.10	-0.53	0.74	-0.35	0.27	-0.13	0.65	0.58	0.71	0.28	0.53	0.13	0.69
Cl	0.08	-0.34	1.00	-0.09	-0.19	-0.24	0.13	0.98	0.19	-0.20	0.21	-0.22	-0.24	-0.28	-0.37	-0.52	0.12
Sc	0.35	-0.02	-0.09	1.00	0.47	0.52	-0.46	-0.21	-0.48	0.28	-0.50	0.19	0.21	0.44	-0.01	0.38	-0.47
Co	-0.21	0.10	-0.19	0.47	1.00	0.33	-0.44	-0.18	0.13	0.84	-0.54	0.47	0.07	0.75	0.32	0.86	-0.54
Ni	-0.09	-0.53	-0.24	0.52	0.33	1.00	-0.84	-0.27	-0.70	0.26	-0.84	-0.19	-0.33	0.21	-0.25	0.49	-0.81
Cu	0.40	0.74	0.13	-0.46	-0.44	-0.84	1.00	0.12	0.48	-0.51	0.99	0.26	0.44	-0.20	0.20	-0.45	0.99
Ga	-0.06	-0.35	0.98	-0.21	-0.18	-0.27	0.12	1.00	0.23	-0.13	0.21	-0.18	-0.22	-0.25	-0.28	-0.53	0.11
Se	-0.35	0.27	0.19	-0.48	0.13	-0.70	0.48	0.23	1.00	0.34	0.44	0.36	0.01	0.23	0.15	-0.08	0.43
As	-0.60	-0.13	-0.20	0.28	0.84	0.26	-0.51	-0.13	0.34	1.00	-0.58	0.47	-0.02	0.81	0.29	0.62	-0.58
Br	0.40	0.65	0.21	-0.50	-0.54	-0.84	0.99	0.21	0.44	-0.58	1.00	0.19	0.41	-0.28	0.16	-0.57	1.00
Rb	0.16	0.58	-0.22	0.19	0.47	-0.19	0.26	-0.18	0.36	0.47	0.19	1.00	0.78	0.81	0.81	0.29	0.23
Sr	0.48	0.71	-0.24	0.21	0.07	-0.33	0.44	-0.22	0.01	0.02	0.41	0.78	1.00	0.42	0.84	0.04	0.44
Y	-0.22	0.28	-0.28	0.44	0.75	0.21	-0.20	-0.25	0.23	0.81	-0.28	0.81	0.42	1.00	0.50	0.54	-0.25
Zr	0.16	0.53	-0.37	-0.01	0.32	-0.25	0.20	-0.28	0.15	0.29	0.16	0.81	0.84	0.50	1.00	0.23	0.18
Nb	-0.07	0.13	-0.52	0.38	0.86	0.49	-0.45	-0.53	-0.08	0.62	-0.57	0.29	-0.04	0.54	0.23	1.00	-0.53
Mo	0.42	0.69	0.12	-0.47	-0.54	-0.81	0.99	0.11	0.43	-0.58	0.99	0.23	0.44	-0.25	0.18	-0.53	1.00
Ag	-0.31	-0.10	-0.34	0.50	0.95	0.52	-0.66	-0.33	-0.03	0.84	-0.75	0.28	-0.10	0.66	0.19	0.90	-0.73
Cd	-0.50	-0.33	-0.23	0.02	0.52	0.10	-0.48	-0.22	0.37	0.63	-0.54	-0.10	-0.45	0.15	-0.06	0.53	-0.53
Sb	-0.36	-0.28	-0.52	0.42	0.64	0.61	-0.73	-0.54	-0.19	0.59	-0.81	-0.16	-0.42	0.29	-0.16	0.80	-0.77
I	-0.06	-0.01	-0.23	0.66	0.93	0.59	-0.60	-0.24	-0.22	0.69	-0.69	0.30	0.01	0.65	0.17	0.88	-0.68
Ba	-0.09	0.39	-0.20	0.10	0.58	-0.13	0.09	-0.13	0.47	0.66	0.03	0.96	0.60	0.85	0.76	0.36	0.06
La	0.04	0.22	-0.29	0.36	0.07	0.31	-0.06	-0.35	-0.42	-0.13	-0.11	-0.31	-0.17	0.03	-0.45	0.22	-0.09
Ce	0.23	0.14	-0.22	0.76	0.82	0.52	-0.46	-0.25	-0.30	0.56	-0.53	0.54	0.36	0.70	0.43	0.75	-0.51
W	-0.26	-0.18	-0.26	0.59	0.92	0.63	-0.73	-0.24	-0.15	0.83	-0.81	0.31	-0.05	0.70	0.21	0.84	-0.79
Tl	-0.26	-0.39	0.27	-0.21	-0.25	-0.03	-0.12	0.24	-0.08	-0.29	-0.10	-0.91	-0.78	-0.67	-0.78	-0.17	-0.14
Pb	0.40	0.65	-0.09	-0.05	-0.25	-0.46	0.68	-0.19	0.17	-0.48	0.63	-0.13	0.06	-0.24	-0.28	-0.11	0.65
Bi	-0.45	-0.21	-0.21	0.43	0.92	0.52	-0.67	-0.19	0.05	0.87	-0.76	0.18	-0.27	0.63	0.01	0.83	-0.75
Ni+Co+Cu	0.21	0.79	-0.11	0.08	0.58	-0.37	0.47	-0.11	0.49	0.33	0.35	0.70	0.48	0.57	0.48	0.47	0.37
CaO+MgO	0.47	0.09	0.15	0.93	0.38	0.29	-0.20	0.01	-0.25	0.18	-0.23	0.24	0.22	0.40	-0.08	0.22	-0.22

This is similar to the model of sulfide formation in the BIF of São Bento of Brazil (Pereira et al., 2007). El Gaby et al. (1988) reported that the BIF and base metal sulphides of the Eastern Desert of Egypt occur exclusively in the Pan-African island arc assemblage and are of equivalent facies, where the iron oxides represent shallow shore environment to the north and the sulphides represent euxinic environment to the south; Umm Nar BIF displays transitional environment. In contrast to the other elements in the association ***(i)***, Ce is distributed parallel to the iron aureole and the axial plane of Umm Nar plunging fold (NW-SE), reflecting its relation to precipitation of iron. However, El Habaak (2004) proposed that cation exchange accompanying the hydration seems to be the most probable reason to explain Ce anomalies in Umm Nar BIF skarn during metasomatism.

ii) Si :

Strong negative correlation of SiO2 with Fe2O2t (r = -0.967) concludes a largely bimodal composition of Ifs. On the other hand, SiO2 is weakly correlated with the main silicate forming oxides, such as Al2O3, Na2O, MgO, and K2O. This indicates that the distribution of SiO2 in Umm Nar BIF is apparently restricted in distribution and merely reflects the occurrence of silica species (such as quartz, chert). However, SiO2 is moderately connected to some elements of the association iv(Cu, r = 0.686; Br, r=0.756 and Mo, r=0.737), showing a possible mobility of these elements within the silica bands.

iii) Na, Al, Mg, P, K, Rb, Y, Ba, Ti, Zr:

Isochemical maps show that elements of this association are not distributed linearly but they apparently erratic distribution, at random and independently of BIF. Their aureoles occur as isolated rounded to ellipsoidal shape (Fig. 21). They are indicative of a probable incorporation of clastic fragments from the host mica schist rocks. The sodium and chloride contents are not correlated with those of iron in the Umm Nar BIF. This argued against the possibility of alkali-(chloride) metasomatism, where hot saline fluids dissolve and transport iron as they move through temperature/pressure gradients and concentrate it in relatively cool, dilute and/or oxidized parts of such systems (Pereira et al., 2007).

iv) Mn, Cu, Mo, V, Sr, Br ± Pb :

Elements of this association are weakly correlated with Fe2O2t, whereas Cu and Mo are moderately correlated with SiO2 (r=0.69 and 0.73). Their occurrence most likely reflects the local high concentration of chalcopyrite and molybdenite. The areal distribution of this element association is remarkably due E-W, that is consistent with the direction of the younger E-W thrust fault (T2) of (El Aref et al. 1993a) and the direction of the dykes exposed at surface of the Um Nar anticline. Therefore, this association seems to be related to both lithologies, corresponding to the intruding dikes and the fault zone.

v) Ca, Sc:

Although aureoles of Ca and Sc have NW-SE direction, the same as those of iron and Si and the axial plane of the Um Nar plunging anticline, these elements are not interrelated with the other elements in BIF deposit. Ca is mostly attributed to calcite laminae that occur within the Fe- and Si-rich bands as it postdated sedimentation of BIFs and formed by alteration of organic matter by magmatic/post magmatic CO2-rich solutions (Salem and Hamdy, 2011).

vi) Cr, Se:

This association does not provide any further information than the specific behavior of Cr and Se. Cr is distinctly enriched than the composition of the upper crust of Condie (1993) (45-52 ppm). Cr and Se exhibit narrow high concentration aureoles conformity with the presence of metagabbro at the southern boundary of the study area. Therefore, this association seems to be related to the lithology, corresponding to the mafic rocks.

5. Integration of Geological, Geochemical and Geophysical Investigations:

Different data of geological, geophysical and geochemical themes are integrated to evaluate Umm Nar BIF deposit, located in the Central Eastern Desert of Egypt, and to prepare a prospectively map for mineral exploration (Fig. 23).

Umm Nar schistis highly deformed forming a tight NW–SE striking and SW dipping overturned anticline plunging very steeply to northwest. Bands of Umm Nar iron formation vary in thickness from few centimeters to a maximum of 5 meters, but the majority do not exceed 1 meter in thickness. They attain maximum thickness at the central part of the deposit (toward the crest of the anticline fold), but at either end they taper out and disappear.

Integration of data from geochemical and geophysical approaches clearly defines the outline of iron ore and its subsurface extension. Residual gravity anomaly map showed main high anomaly taking the same direction of the exposed iron bands. Intensity of this anomaly increases to the crest of the anticline fold, pointing to subsurface extension of the exposed BIF. The total intensity magnetic map reveals that main high magnetic anomaly occupies the central and northern parts of the map which is compatible with the surface iron ore in the main body and crest of BIF anticline fold.

Data integration permits definition of at least three distict faulting directions (NW-SE, NE-SW and E-W) within the iron body. These faults were plotted between the abrupt changes of the geophysical anomalies.

The geochemical results reveal sites or clusters of sites containing anomalously high concentration of iron. Prominent iron concentrations were associated with WNW-ESE striking aureoles of Co, Ni, Ag, Nb, Sb, I, Ce, W, As. These elements represent a pervasive hydrothermal sulfidation (mainly arsenopyrite) of Fe-

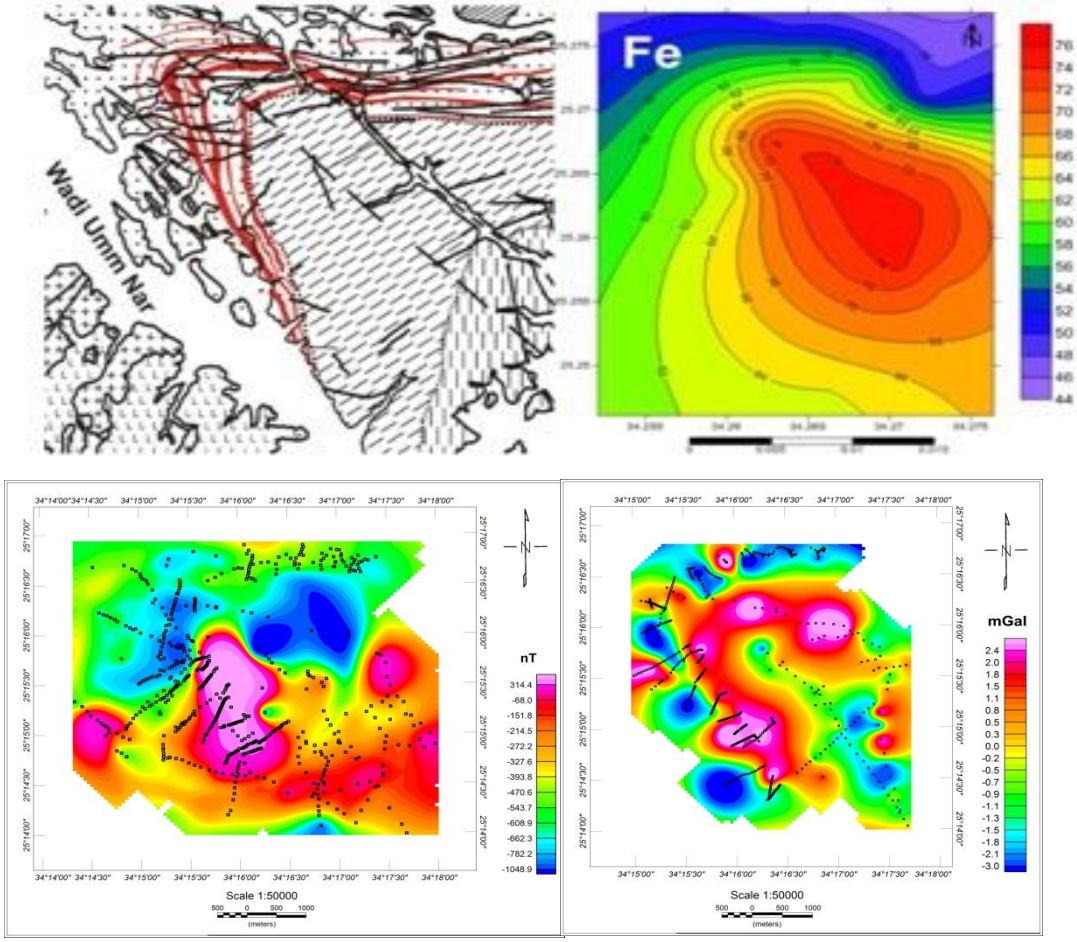

Fig. 23: Geological map, Isochemical map , Total intensity magnetic map and Residual gravity map of Umm Nar, respectively.

rich bands and sign for gold deposition. E-W dykes and lineaments in the study area, probably acts as channel for aureols of Mn, Cu, Mo, V, Sr, Br± Pb.

However, multi-classification of the prospect for detailed study could increase the resolution of the prospectivity map and decrease the drilling risk.

6. SUMMARY AND CONCLUSIONS

The link between geophysical investigation of Umm Nar area in the form of gravity and magnetic survey from one side, and the geochemical investigation in the other side, concluded some important results. The outcome of this integrated study can be summarized in the following items:

1- Qualitatively, residual anomaly gravity map of Umm Nar iron ore delineates three sets of subsurface faults trending NE-SW, NW-SE and E-W.

2- Combination of residual anomaly gravity and total magnetic intensity maps, high anomaly areas were identified. These areas are identical and compatible with surface beds bearing BIF and eliminate away from the anticlinal BIF fold. South western part of these high anomalies is related to gabbroic pluton.

3- Quantitatively, Depth of the source body was estimated up to 350 meter using Tikhonov regularized downward continuation which could effectively help in the estimation of the depths to the researched near surface gravity and magnetic sources.

4- Based on petrographical and XRD investigations, most abundant ferriferous minerals are magnetite and hematite, associated with varying amounts of quartz, goethite, garnet, amphibole and calcite.

5- Geochemical analysis for the collected surface samples showed high concentration of iron reaching to 75% matching in the areas of high gravity and magnetic anomalies.

6- The Pearson linear correlation matrices divide elements into six associations: *i)* Fe, Co, Ni, Ag, Nb, Sb, I, Ce, W, As, *ii)* Si, *iii)* Na, Al, Mg, P, K, Rb, Y, Ba, Ti, Zr , *iv)* Mn, Cu, Mo, V, Sr, Br ± Pb, *v)* Ca, Sc, *vi)* Cr, Se. Geochemical mapping that used to identify structural metals controlling

mineralization showed different orientations of metals associated with NW-SE, WNW-ESE faulting.

7- The recorded high Hg values in association Sb in surface samples lead to the presence of gold accumulation at deeper level.

Acknowledgement

We are thankful to the Academy of Scientific Research and Technology for financial and technical support to complete this research. Many thanks also must go to Prof. Dr. Hans J. Götze, Institut für Geowissenschaften, Christian-Albrechts-Universität zu Kiel, for continuous advice and helping in 3d-density modeling. All my gratitude to all members of the gravity department in Christian-Albrechts-Universität zu Kiel, Germany, for their kind hospitality and help.

REFERENCES

Abu El-Ata, A.S.A. & Saleh, A. (2002): Magnetic prospection of the manganese occurrences of Abu Ramad area, southern Eastern Desert, Egypt. Geophysics and Geodesy, 32/1.

Adams, D., (2006): Geochemical Sampling and Geostatistics Notes, Delta Mine TrainingCenter;http://www.dmtcalaska.org/course_dev/explogeo/class12/notes12.html (accessed December 10, 2006). 2011, pp. 583-593.

Attia, M.I., (1950): The geology of iron ore-deposits of Egypt. Geol. Surv., Cairo, Egypt, p34.

Basta, F.F., Maurice, A.E., Fontboté, L. & Favarger, P.Y. (2011): Petrology and geochemistry of the banded iron formation (BIF) of Wadi Karim and Um Anab, Eastern Desert, Egypt: Implications for the origin of Neoproterozoic BIF. Precambian Research, 187: 277-292.

Bostrom, K., (1973): The origin and fate of ferromanganoan active ridge sediments. Stockholm Contribution of Geology, 27: 149-243.

Condie K.C. (1993) :Chemical composition and evolution of the upper continental crust: Contrasting results from surface samples and shales [J]. Chemical Geology. 104, 1-37.

Dasgupta, N., McGhee, D.E., Greenwald, A.G., & Banaji, M. R. (1999): Automatic preference for White Americans: Does the frequency of race stimuli produce the effect? Unpublished manuscript, New School University.

E1 Gaby, S., List, F.K. & Tehrani, R., (1988): Geology evolution and metallogenesis of the Pan-African belt in Egypt. In: E1 Gaby, S., Greiling, R.O. (eds.) The Pan-African belt of northeast Africa and adjacent areas. Vieweg, Braunschweig, 17-68.

El Aref, M.M., Abdel Wahed, M., El Dougdoug, A. & El Manawi, A.W. (1993a): Geologic setting and deformational history of Umm Nar BIF and associated rocks, Eastern Desert. Egypt. J. Geol, 37(2): 205-230.

El Aref, M.M., El Dougdoug, A.A. & Mesaed, A.A. (1993b): Petrography and diagensis of the high-lying ferricretes of El Bahariya Depression, Western Desert, Egypt. Egypt Mineralogist, 4: 23-53.

El Habaak, G.H., (2004): Pan-African skarn deposits related to banded iron formation, Um Nar area, Central Eastern Desert, Egypt. Journal of African Earth Sciences, 38: 199–221.

El-Ramly, M.F., El-Akaad, M.K. & Shaaban, M.S., (1963): Geology and structure of the iron-ore deposits of Gebel El-Hadeed, Eastern Desert. Geol, Survey and Mineral Research Dept., Cairo, Egypt, paper no.16, p 31.

Ewers, W.E. & Morris, R.C., (1981): Studies on the Dales Gorge member of Brockman iron formation. Economic Geology, 76: 1929–1953.

Fortin, D. & Langley, S., (2005): Formation and occurrence of biogenic iron-rich minerals. Earth Sci. Rev, 72: 1-19.

Harris, J.R., Wilkinson, L. & Grunsky, E.C., (2000): Effective Use and Interpretation of Lithogeochemical Data in Regional Mineral Exploration Programs: Application of Geographic Information Systems (GIS) Technology. Ore Geology Reviews, **16:** 107-143.

Hussein, A.A. & E1 Sharkawi, M.A., (1990): Mineral deposits. In: Said, R. (ed.) The Geology of Egypt. Balkema, Rotterdam, 511-566.

James, H.L., (1992): Precambrian iron-formations: nature, origin, and mineralogic evolution from sedimentation to metamorphism. In: Wolf, K.H., Chilingarian, G.V. (Eds.), Diagensis III.Developments in Sedimentology, 47: 543-589.

Ilyin, A.V., (2009): Neoproterozoic Banded Iron Formations. Lithology and Mineral Resources, 44: 78-86.

Klein, C., (2005): Some Precambrian banded iron-formations (BIFs) from around the world: Their age, geologic setting, mineralogy, metamorphism, geochemistry, and origin. The American Mineralogist, 90: 1473-1499.

Klein, C. and Beukes, N., (1993): Sedimentology and geochemistry of the glaciogenic Rapitan iron formation in Canada. Economic Geology, 88: 542-565.

Loizenbauer, J., Wallbrecher, E., Fntz, H., Neumayr, P., Khudeir, A. A. & Kloetzil, U., (2001): Structural geology, single zircon ages and fluid inclusion studies of the Meatiq metamorphic core complex. implications for Neoproterozoic tectonics in the Eastern Desert of Egypt. Precambrian Research, **110:** 357-383.

Lottermoster, B. & Ashley, P., (2000): Geochemistry, petrology and origin of Neoproterozoic ironstones in the eastern part of the Adelaide

Geosyncline, South Australia. Precambrian Research, 101: 49-67.

Manikyamba, C. & Naqvi, S., (1995): Geochemistry of Fe-Mn formations of the Archaean Sandur schist belt, India - mixing of clastic and chemical processes at a shallow shelf. Precambrian Research, 72: 69-95.

Murray, R., Brink, M., Gerlach, D., Russ, G. & Jones, D., (1991): Rare earth, major and trace elements in chert from the Franciscan complex and Monterey Group, California: Assessing REE sources to fine grained marine sediments. Geochimica et Cosmochimica Acta, 55: 1875-1895.

McClenaghan, M.B., Thorleifson, L.H. & DiLabio, R.N.W., (1997): Till geochemical and indicator mineral methods in mineral exploration; In: Proceedings of Exploration 97:Fourth Decennial International Conference on Mineral Exploration, (ed.) Gubins A G, Prospectors & Developers Association of Canada, pp. 233-248.

Mekkawi, M.M., (2012): Application of magnetic method mineral exploration iron ore deposit, South Zagros suture zone, Iraq. EGS Journal, **10(1):** 117-124.

Nabighian, M.N., Ander, M.E., Grauch, V.J.S., Hansen, R.O., LaFehr, T.R., Li, Y., Pearson, W.C., Peirce, J.W., Phillips, J.W. & Ruder, M.E., (2005): Historical development of the gravity method in exploration. Geophysics, 70(6): 63-89.

Pašteka, R., Karcol, R., Kušnirak, D.A. &Mojzeš, A., (2012): REGCONT: A Matlab based program for stable downward continuation of geophysical potential fields using Tikhonov regularization. Computers & Geosciences, 49: 278–289.

Pearce, J.A., Barker, P.F., Edwards, S.J., Parkinson, I.J., Leat, P.T., (2000): Geochemistry and tectonic significance of peridotites from the South Sandwich Arc-basin Systems, South Atlantic. Contributions to Mineralogy and Petrology, **139:** 36–53.

Pereira, S.L.M., Lobato, L.M., Ferreira, J.E. & Jardim, E.C., (2007): Nature and origin of the BIF-hosted São Bento gold deposit, Quadrilátero Ferrífero, Brazil, with special emphasis on structural controls. Ore Geology Reviews, **32:** 575-591.

Salem, I.A., Hamdy, M.M., (2011): Stable carbon isotope, organic carbon and carbonate mineralogical characteristics of BIFs from Central Eastern Desert of Egypt: Reconnaissance study for a Neoproterozoic carbon cycle. Egyptian Journal of Geology, v.55,2011, p.431-446.

SIMS, M.A., & JAMES, H.L. (1984): Banded iron ore formation of Late Proterozoic age in the Central 885 Eastern desert, Egypt: geological and tectonic setting. Economic Geology, 79, 1777-1784.

Stern, R. J., Johanson, P.R., Kroner, A. & Yibas, B., (2004): Neoproterozoic ophiolites of the Arabian-Nubian Shield. In: Kusky TM (ed) Precambrian ophiolites and related rocks. Developments in Precambrian geology, **13:** 95–128.

Tikhonov A.N., Glasko V.B., Litvinenko O.K. & Melichov V.P., (1968): Analytic continuation of a potential in the direction of disturbing masses by the regularization method. Izv, Earth Physics, 12: 30–48 (in Russian; English translation: 738–747).

Wedepohl, K.H. and Hartmann, G. (1994): The composition of the primitive upper earth's mantle. In: Kimberlites, related rocks and mantle xenoliths. Meyer, H.O.A. and Leonardos, O.H. (Editors), Companhia de Pesquisa de Recursos Minerais, Rio de Janeiro. 1: 486-495.

Wonder, J.D., Spry, P.G., and Windom, K.E. (1988): Geochemistry and origin of manganese-556 rich rocks related to iron-formation and sulfide deposits. Economic Geology, 83, 1070-557 1081.